

The virtual observatory service TheoSSA: Establishing a database of synthetic stellar flux standards

I. NLTE spectral analysis of the DA-type white dwarf G191–B2B★ ★★ ★★

T. Rauch¹, K. Werner¹, R. Bohlin², and J. W. Kruk³

¹ Institute for Astronomy and Astrophysics, Kepler Center for Astro and Particle Physics, Eberhard Karls University, Sand 1, 72076 Tübingen, Germany,
e-mail: rauch@astro.uni-tuebingen.de

² Space Telescope Science Institute, 3700 San Martin Drive, Baltimore, MD 21218, USA

³ NASA Goddard Space Flight Center, Greenbelt, MD 20771, USA

Received 22 July 2013 / Accepted 22 August 2013

ABSTRACT

Context. Hydrogen-rich, DA-type white dwarfs are particularly suited as primary standard stars for flux calibration. State-of-the-art NLTE models consider opacities of species up to trans-iron elements and provide reliable synthetic stellar-atmosphere spectra to compare with observation.

Aims. We will establish a database of theoretical spectra of stellar flux standards that are easily accessible via a web interface.

Methods. In the framework of the Virtual Observatory, the German Astrophysical Virtual Observatory developed the registered service TheoSSA. It provides easy access to stellar spectral energy distributions (SEDs) and is intended to ingest SEDs calculated by any model-atmosphere code. In case of the DA white dwarf G191–B2B, we demonstrate that the model reproduces not only its overall continuum shape but also the numerous metal lines exhibited in its ultraviolet spectrum.

Results. TheoSSA is in operation and contains presently a variety of SEDs for DA-type white dwarfs. It will be extended in the near future and can host SEDs of all primary and secondary flux standards. The spectral analysis of G191–B2B has shown that our hydrostatic models reproduce the observations best at $T_{\text{eff}} = 60\,000 \pm 2000$ K and $\log g = 7.60 \pm 0.05$. We newly identified Fe vi, Ni vi, and Zn iv lines. For the first time, we determined the photospheric zinc abundance with a logarithmic mass fraction of -4.89 ($7.5 \times$ solar). The abundances of He (upper limit), C, N, O, Al, Si, O, P, S, Fe, Ni, Ge, and Sn were precisely determined. Upper abundance limits of about 10 % solar were derived for Ti, Cr, Mn, and Co.

Conclusions. The TheoSSA database of theoretical SEDs of stellar flux standards guarantees that the flux calibration of all astronomical data and cross-calibration between different instruments can be based on the same models and SEDs calculated with different model-atmosphere codes and are easy to compare.

Key words. Standards – Stars: abundances – Stars: atmospheres – Stars: individual: G191–B2B – Stars: white dwarfs – Virtual observatory tools

1. Introduction

In the framework of the Virtual Observatory (VO), the German Astrophysical Virtual Observatory (GAVO) project provides synthetic stellar spectra on demand via the registered Theoretical Stellar Spectra Access (TheoSSA) VO service (Rauch 2008a; Rauch & Nickelt 2009; Rauch et al. 2009). These SEDs can be used for spectral analyses (Rauch et al. 2010; Ringat & Rauch 2010; Rauch & Ringat 2011; Ringat et al. 2012) or serve as ionizing spectra for e.g. photoionization models of ionized

nebulae. The registered TMAW VO tool¹, that allows to calculate individual NLTE model atmospheres considering opacities of H, He, C, N, O, Ne, Na, and Mg, provides additional SEDs which are automatically ingested by TheoSSA. Figure 1 shows the complete action scheme for a VO user to retrieve an SED.

With the increasing usage of TheoSSA over the last years, it became necessary to demonstrate the reliability of the SEDs. We established simple benchmark tests (Ringat et al. 2012) to show the achievable analysis precision, e.g. in the determination of effective temperatures (T_{eff}) and surface gravities ($\log g$), in cases that TMAW SEDs are used which are calculated with standard model atoms that are limited in the number of atomic levels treated in NLTE. This guarantees model calculations in a reasonable time for a VO user.

Since 2012 TheoSSA also includes synthetic spectra of spectrophotometric standard stars. In this paper, we start to systematically establish a database of these and address the reliability

* Based on observations with the NASA/ESA Hubble Space Telescope, obtained at the Space Telescope Science Institute, which is operated by the Association of Universities for Research in Astronomy, Inc., under NASA contract NAS5-26666.

** Based on observations made with the NASA-CNES-CSA Far Ultraviolet Spectroscopic Explorer.

*** Figures A.1 and A.2 are available in electronic form at <http://www.aanda.org> (they are also available at the CDS in FITS format).

¹ Tübingen Model-Atmosphere WWW Interface, <http://astro.uni-tuebingen.de/~TMAW>

of state-of-the-art model-atmosphere spectra and the achievable limits in future flux calibration.

Table 1. Parameters of the HST DA standard stars (Gianninas et al. 2011).

name	WD no. ^a	T_{eff} [K]	$\log g$ [cm/sec ²]
G191–B2B	0501+527	$60\,920 \pm 993$	7.55 ± 0.05
GD 71	0549+158	$33\,590 \pm 483$	7.93 ± 0.05
GD 153	1254+223	$40\,320 \pm 626$	7.93 ± 0.05
HZ 43A ^b	1314+293	$56\,800 \pm 1249^c$	7.89 ± 0.07

Notes.

^(a) WD numbers are from McCook & Sion (1999). ^(b) HZ 43A is only used in the UV because of contamination at longer wavelengths from its M-dwarf companion. ^(c) Beuermann et al. (2006, 2008) determined $T_{\text{eff}} = 51\,111 \pm 660$ K and $\log g = 7.90 \pm 0.080$.

White dwarfs (WDs) are ideal objects for the calibration of astronomical observations (Rauch 2012). They are relatively simple objects and their radiation is determined by fundamental physics, e.g. their radius is defined by electron degeneracy. Moreover, they are nearby and their distance can be measured precisely, at least by the upcoming GAIA² mission (cf. Pancino et al. 2012, for a description of the GAIA spectrophotometric standard stars survey). Most of the hot, hydrogen-rich WDs (spectral type DA) with $T_{\text{eff}} < 40\,000$ K have virtually pure hydrogen atmospheres (gravitational settling), while the hotter WDs exhibit lines of heavier elements due to radiative levitation. WD spectral modeling requires adequate observations (WDs are intrinsically faint) and state-of-the-art theoretical model atmospheres that account for reliable physics and deviations from local thermodynamic equilibrium (LTE).

The hot DA-type WD G191–B2B (BD+52°913) is, together with GD 71, and GD 153, one of the primary flux reference standards for all absolute calibrations from 1000 to 25 000 Å (Bohlin 2007). Recent results for their T_{eff} and $\log g$ are summarized in Table 1. G191–B2B, the hottest and visually brightest ($m_V = 11.7228$, van Leeuwen 2007) isolated WD (with a well known distance of 57.96 pc, Anderson & Francis 2012) of the sample, is ideal for panchromatic calibration from the ultraviolet (UV) to the infrared (IR) wavelength range. However, due to its high T_{eff} and relatively low $\log g$, radiative levitation competes against gravitational settling and holds trace elements in the photosphere and exhibits many weak metal lines (e.g. Barstow et al. 2003) in its observed UV spectrum.

A variety of previous spectral analyses of G191–B2B (Table 2) had shown that it is difficult to determine its T_{eff} precisely. Barstow et al. (1998) found that the metal content in the photosphere has a strong impact on the determined T_{eff} . $T_{\text{eff}} = 60\,920$ K was found by the most recent analysis (Gianninas et al. 2011) who considered only C, N, and O (at solar abundances) in their models. The neglect of other metals calls for improved models with better metal opacities. The same may be true for HZ 43A even if metals are below the detection limit of the available spectra (Table 1).

Many abundance analyses were performed, most of them (e.g. Barstow et al. 2005), were based on previous T_{eff} determinations from Balmer-line fits (cf. Table 2) and not from self-consistent fits to models with varying metal abundances. Lanz

et al. (1996) measured He, C, N, O, Si, Fe, and Ni abundances, Holberg et al. (2003) determined abundances of C, N, O, Al, Si, Fe, and Ni and gave upper limits for Mg, Cr, Mn, and Co. The compiled abundances are listed in Table 3.

Table 3. Abundances of photospheric trace elements in G191–B2B from previous analyses. Table 2 displays the T_{eff} and $\log g$ values of the employed models.

element	log mass fraction	
He	-4.2 ± 0.1^a	-4.4^i
	-4.4 ± 0.3^b	
C	-4.6 ± 0.3^c	-5.6^i
	-4.6 ± 0.3^b	
N	-4.3 ± 0.4^d	-5.9^i
	-5.6 ± 0.3^b	
O	-4.8 ± 0.3^e	-4.6^i
	-4.8 ± 0.3^b	
Mg		$< -5.6^i$
Al		-5.1^i
Si	-5.1 ± 0.4^d	-5.0^i
	-5.1 ± 0.5^c	
P	-5.0 ± 0.3^b	
	-6.2 ± 0.2^c	
S	-5.2 ± 0.5^c	
	$< -7.0^b$	
Cl		
Cr		$< -6.3^i$
Mn		$< -6.3^i$
Fe	-3.8 ± 0.3^d	-3.8^i
	-3.4 ± 0.4^f	
	-3.3 ± 0.3^b	
Co		$< -6.2^i$
Ni	-4.2 ± 0.5^g	-4.4^i
	-4.2 ± 0.4^f	
Ge	-3.9 ± 0.3^b	
	-6.1 ± 0.2^h	
Sn	-6.9 ± 0.2^h	

Notes.

^(a) Crudace et al. (2002) ^(b) Lanz et al. (1996) ^(c) Vennes et al. (1996) ^(d) Vidal-Madjar et al. (1994) ^(e) Chayer et al. (1996) ^(f) Werner & Dreizler (1994) ^(g) Holberg et al. (1994) ^(h) Vennes et al. (2005) ⁽ⁱ⁾ Holberg et al. (2003), He abundance assumed, no abundance uncertainties given

Based on a grid of state-of-the-art line-blanketed NLTE model atmospheres that include opacities of all identified metals, we perform a detailed spectral analysis. We describe the available observations in Sect. 2, followed by a brief introduction to our model atmosphere code and the atomic data (Sect. 3). The spectral analysis is summarized in Sect. 4 and we end with our conclusions (Sect. 7).

2. Observations

2.1. FUSE data

G191–B2B was observed many times over the course of the FUSE mission in the wavelength range 910 Å – 1190 Å, both for calibration purposes and for studies of the interstellar medium. For the present study, only observations obtained in the first eight months of the mission through the LWRS spectrograph aperture were analyzed. This time period included the majority of the LWRS exposure time obtained during the mission, and

² http://www.esa.int/Our_Activities/Space_Science/Gaia_overview

Table 2. T_{eff} and $\log g$ from previous analyses of G191–B2B.

T_{eff} [K]	$\log g$ [cm/sec ²]	reference	method
61 900	7.5 ^a	Shipman (1979)	LTE, pure H, optical colors
56 788 ± 3336	5.95 ± 0.04	Koester et al. (1979)	LTE, pure H, optical colors ^b
62 250 ± 3520	7.55 ± 0.35	Holberg et al. (1986)	LTE, pure H, H ₁ L α line
59 250 ± 2000	7.50 ± 0.10	Kidder 1990 cited by Holberg et al. (1991)	LTE, pure H, H ₁ H γ and H δ lines
61 000 ⁺⁶⁰⁰⁰ -4000	8.00 ^a	Green et al. (1990)	LTE, H+He, extreme ultraviolet (EUV) continuum
61 170 ⁺⁴⁸³⁰ -4230	8.00 ^a	Finley et al. (1990)	LTE, H+He, ultraviolet (UV) continuum
62 250 ± 1000	8.00 ^a	Finley et al. (1990)	LTE, H+He, H ₁ L α line
62 250	7.55	Vennes et al. (1991)	NLTE, H+HeCNSi, UV spectrum
53 500 ± 500	7.50 ^a	Koester & Finley (1992)	LTE, H+He ^c , UV continuum
60 500 ± 900	7.50 ± 0.05	Vidal-Madjar et al. (1994)	LTE, H+He, H ₁ Balmer lines
57 900 ± 1500	7.50 ^a	Dupuis et al. (1995)	NLTE, pure H, EUV continuum ^d
54 000 ± 800	7.50 ^a	Dupuis et al. (1995)	NLTE, H+CNOFe, EUV continuum ^d
60 500 ± 1000	7.5	Lanz et al. (1996)	LTE, H+HeC, H ₁ Balmer lines
56 000 ± 1000	7.5	Lanz et al. (1996)	NLTE, H+HeC, H ₁ Balmer lines
55 200 ± 1000	7.5	Lanz et al. (1996)	NLTE, H+HeCFe, H ₁ Balmer lines
64 000 ± 1000	7.64 ± 0.06	Vennes et al. (1996)	LTE, pure H, H ₁ Lyman lines
57 900 ± 1500	7.5	Vennes et al. (1996)	LTE, pure H, extreme UV (EUV) continuum ^d
64 100 ± 700	7.69 ± 0.04	Vennes et al. (1996)	LTE, H+CNOFe, H ₁ Balmer lines
52 600 ± 800	7.53 ± 0.07	Vennes et al. (1996)	LTE, H+CNOFe, H ₁ Lyman lines
54 000 ± 800	7.5	Vennes et al. (1996)	LTE, H+CNOFe, EUV continuum ^d
61 193 ± 241	7.49 ± 0.01	Finley et al. (1997)	LTE, H-Ni, H ₁ Balmer lines
59 160 ⁺¹²⁷⁰ -1070	7.36 ^{+0.08} -0.07	Barstow et al. (1998)	NLTE, pure H, H ₁ Balmer lines
59 190 ⁺¹⁴⁰⁰ -820	7.36 ^{+0.07} -0.07	Barstow et al. (1998)	NLTE, H+He, H ₁ Balmer lines
59 060 ⁺¹¹³⁰ -1090	7.36 ^{+0.08} -0.07	Barstow et al. (1998)	NLTE, H+He + heavy-metal poor, H ₁ Balmer lines
53 840 ⁺⁴⁰⁰ -160	7.38 ^{+0.07} -0.08	Barstow et al. (1998)	NLTE, H+He + heavy-metal rich, H ₁ Balmer lines
52 920 ± 350	7.36 ± 0.03	Barstow et al. (1998)	NLTE, H+He + heavy-metal rich, H ₁ Lyman lines ^e
56 000	7.6	Wolff et al. (1998)	LTE + NLTE, H+CNOSiFeNi, EUV continuum ^d
56 000	7.6	Dreizler & Wolff (1999)	NLTE, H+CNOSiFeNi, diffusion model, EUV to optical
54 600 ± 200	7.60 ± 0.02	Barstow et al. (2001)	NLTE, H+HeCNOSiFeNi, H ₁ Balmer lines
52 930 ± 3600	7.16 ± 0.2	Barstow et al. (2001)	NLTE, H+HeCNOSiFeNi, H ₁ Lyman lines ^f
53 180 ± 530	7.43 ± 0.04	Barstow et al. (2001)	NLTE, H+HeCNOSiFeNi, H ₁ Lyman lines ^e
56 000	7.59	Schuh et al. (2002)	NLTE, H+HeCNOSiFeNi, diffusion model, EUV continuum ^d
54 000	7.5	Holberg et al. (2003)	NLTE, metal lines
58 865 ± 706	7.57 ± 0.038	Lajoie & Bergeron (2007)	NLTE ^g , pure H, H ₁ Balmer lines
60 680 ± 15 000	7.57 ^h	Lajoie & Bergeron (2007)	NLTE ^g , pure H, H ₁ Lyman lines ⁱ
57 414 ± 4700	7.57 ^h	Lajoie & Bergeron (2007)	NLTE ^g , pure H, V-normalization method
61 980 ± 514	7.56 ± 0.04	Allende Prieto et al. (2009)	NLTE, H ₁ , H ₁ Balmer lines
60 920 ± 993	7.55 ± 0.05	Gianninas et al. (2011)	NLTE, H+CNO, H ₁ Balmer lines ^k

Notes.

(^a) Assumed $\log g$ value. (^b) The authors note that the results are extrapolated from their model grid. (^c) Stratified model, hydrogen-layer mass between 6×10^{-15} and $8 \times 10^{-15} M_{\odot}$. (^d) Extreme Ultraviolet Explorer (EUVE, <http://heasarc.gsfc.nasa.gov/docs/euve/euve.html>) observations. (^e) Orbiting and Retrievable Far and Extreme Ultraviolet Spectrometer (ORFEUS, <http://www.uni-tuebingen.de/en/4221>) and FUSE observations. (^f) Hopkins Ultraviolet Telescope (HUT, <http://praxis.pha.jhu.edu/>) observations. (^g) International Ultraviolet Explorer (IUE) observations. (^h) Adopted from their optical solution. (ⁱ) Models described in Liebert et al. (2005). (^j) The authors note that T_{eff} may be overestimated by ≈ 6000 K because their pure-H models are inappropriate due to the photospheric metal content. (^k) New H₁ Stark line-broadening tables from Tremblay & Bergeron (2009).

had the secondary benefit that the detectors had not yet suffered much degradation from gain sag. The observation IDs of the datasets were: M1010201, M1010202, M1030602, P1041203, and S3070101.

Apart from a few quirks affecting the M1010201 and M1030602 observations, which were among the first obtained during the mission, the quality of the data is excellent. No SiC data were obtained in observations M1010201 or M1030602

as a result of channel mis-alignment. Otherwise: exposure-to-exposure variations in flux were typically well under 1 %, indicating good channel alignment. The detector region used to record spectral image data for LiF2b was offset from the actual spectrum position in the M1010201 observation, so those spectra were discarded. The net exposure times were 33.3 ksec for the SiC channels, 36 ksec for LiF2b, and 40 ksec for LiF1 and LiF2a.

No special processing was applied to data from individual exposures. Raw data were processed with CalFUSE v3.2.3. Zero-point offsets in the wavelength scale were adjusted for each exposure by shifting each spectrum to coalign narrow interstellar absorption features. In order to assess the influence of geocoronal airglow emission, spectra obtained during orbital day and night were combined separately. All the observations were obtained in spectral image (“histogram”) mode, so no information on photon arrival time was available within an exposure. However, the timeline table in the intermediate data files was examined for each exposure to determine the time spent in the “Day” and “Night” portions of the orbit. If the “Day” portion of such an exposure exceeded 15 % of the total exposure duration, it was included with the other Day spectra. Because histogram mode exposures were short, most exposures were entirely Day or entirely Night.

The individual exposures from all five observations were then combined to form composite Day and Night spectra for each channel. The Day and Night spectra were then compared at the locations of all the known airglow emission lines. If the Day spectra showed any excess flux in comparison to the Night spectra at those locations, the corresponding pixels in the Day spectra were flagged as bad and were not included in subsequent processing. Significant airglow emission during orbital Day was seen for most observations at H_I Ly β through Ly δ , and O_I $\lambda\lambda$ 988, 1027, 1028, 1039 Å. Significant airglow was present during orbital night only at Ly β ; this affects the interstellar absorption profile but has no effect on our analysis of the photospheric spectrum.

The final step was to combine the spectra from the four instrument channels into a single composite spectrum. Because of residual distortions in the wavelength scale in each channel, additional shifts of localized regions of each spectrum were required to coalign the spectra; such shifts were typically only one or two pixels. Bad pixels resulting from detector defects were flagged at this point and excluded from further processing. Finally, the spectra were resampled onto a common wavelength scale and combined, weighting by signal to noise on a pixel-by-pixel basis.

The signal to noise of the final combined spectrum is limited by fixed-pattern noise in the detectors. The final spectrum has a minimum of roughly 20 000 counts per 0.013 Å pixel in the continuum, near the Lyman edge, and 60 000 - 130 000 counts per pixel long-ward of 1000 Å. The effects of fixed-pattern noise are minimized by the fact that the positions of the spectra on the detectors varied during each observation, and by the fact that nearly every wavelength bin was sampled by at least two different detectors.

2.2. HST data

As described in detail by Bohlin & Gordon (in prep.), the HST/STIS low-dispersion flux calibration is derived from an ensemble match to the NLTE TLUSTY (version 203) model atmosphere SEDs for pure hydrogen (Hubeny & Lanz 1995). The models are for G191–B2B, GD 71, and GD 153. Originally, HZ 43A was also used as a standard star but fell off the list of primary flux standards because of an M star companion that contaminates the STIS observations in the visible and IR (Bohlin et al. 2001).

For the STIS échelle modes, the flux calibration is based only on the TLUSTY model for G191–B2B. The échelle absolute fluxes are less precise than for low dispersion because of

the single model for the reference fluxes, because of imprecision in the matching of the separate échelle orders, and because the plethora of weak lines at the shorter wavelengths are missing in the reference SED. However, the STIS échelle narrow metal line profiles are unaffected by uncertainties in the absolute fluxes.

For the highest STIS resolution of ≈ 3 km/s, there are two modes, namely E140H and E230H, which require several central wavelength settings for complete wavelength coverage from 1145 – 3145 Å. Because G191–B2B is the primary STIS échelle calibration star with repeated observations, 105 observations in the $0''.2 \times 0''.2$ aperture are available from the Mikulski Archive for Space Telescopes (MAST)³. Each spectrum is resampled to a wavelength grid with a sampling interval corresponding to a resolving power of $R = 2.3 \times 10^5$ and co-added. The number of individual observations at each wavelength point ranges from 4 – 44, while the total exposure time ranges from 6400 – 64 000 s at each point. The total counts in electrons at each point in the continuum are typically well above 1000 and range up to over 10 000 from 1225 – 1400 Å, where the statistical uncertainty is sometimes better than 1 %. The high-dispersion échelle spectrum is available from the CALSPEC⁴ database along with the STIS low-dispersion data.

The photospheric radial velocity $v_{\text{rad}} = 22.1 \pm 0.6$ km/s measured by Holberg et al. (1994) matches well our STIS observation. We adopt this value for our analysis.

2.3. Interstellar line absorption and reddening

The interstellar neutral hydrogen density N_{H_1} was determined from the comparison of our final model with the STIS and FUSE observations (Fig. 2). In all plots shown in this paper, we modeled the interstellar medium (ISM) line absorption (using Voigt line profiles) with WRPLOT⁵. The best match is found for $\log(N_{\text{H}_1} / \text{cm}^2) = 18.34^{+0.08}_{-0.10}$. The D_I blends to H_I L α - δ are clearly visible and best reproduced at $\log(N_{\text{D}_1} / \text{cm}^2) = 13.54^{+0.05}_{-0.06}$, i.e. D/H = $1.59^{+0.41}_{-0.65} \times 10^{-5}$. Our values are in good agreement with those determined by Lemoine et al. (2002), $\log(N_{\text{H}_1} / \text{cm}^2) = 18.18 \pm 0.18$ and D/H = $1.66^{+0.9}_{-0.6} \times 10^{-5}$ (both with 2σ errors).

Besides H_I and D_I, we identified interstellar lines of C_{II} - IV, N_I - II, O_I, Al_{II}, Si_{II} - III, P_I - II, S_I - II, and Fe_{II} in the FUSE and STIS spectra (Table 5). To identify pure photospheric lines that are contaminated by ISM lines, we modeled all of these and found that we need two distinct clouds with $v_{\text{rad}} = 9 \pm 1$ km/s and $v_{\text{rad}} = 19 \pm 1$ km/s. This is well in agreement with the measurements of Sahu et al. (8.6 ± 1.7 km/s and 19.3 ± 2.5 km/s 1999), who assigned the latter value to the local interstellar cloud. Dickinson et al. (2012b) measured 8.5 ± 0.18 km/s and 19.3 ± 0.03 km/s. They unambiguously detected that the first cloud is of circumstellar origin. An additional third cloud with intermediate velocity like assumed by Vidal-Madjar et al. (1998, $v_{\text{rad}} = 8.2, 13.2, 20.3 (\pm 0.8$ km/s) is not necessary for our modeling (Fig. 3, top).

Interestingly, we find additional weak absorptions of O_I $\lambda 1302.163$ Å and N_I $\lambda 1199.550, 1200.223, 1200.710$ Å at v_{rad} of -26.3 , km/s and -26.1 , km/s, respectively. These velocities are reminiscent of the expansion velocity of a planetary nebula shell (e.g.. Kwok et al. 1978), that for a stellar mass of

³ <http://archive.stsci.edu/>

⁴ <http://www.stsci.edu/hst/observatory/cdbs/calspec.html>

⁵ <http://www.astro.physik.uni-potsdam.de/~htodt/wrplot/index.html>

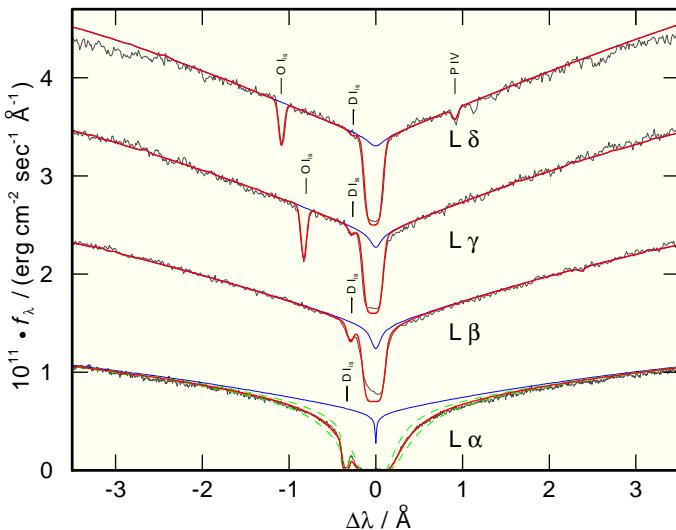


Fig. 2. Comparison of STIS and FUSE observations around $\text{H}_1 \text{L} \alpha - \delta$ with our final model. Thick (red in the online version) photospheric + ISM line absorption model with $N_{\text{H}_1} = 2.2 \times 10^{18} \text{ cm}^{-2}$, thin (blue) pure photospheric model; dashed (green, $\text{L} \alpha$ only) $N_{\text{H}_1} = 1.2 \times 10^{18} \text{ cm}^{-2}$, $3.2 \times 10^{18} \text{ cm}^{-2}$. The locations of the D_1 blends are marked. $\text{L} \beta - \delta$ are shifted in flux ($0.7, 1.6, 2.7 \times 10^{-11} (\text{erg cm}^{-2} \text{s}^{-1} \text{\AA}^{-1})$) for clarity. A reddening of $E_{B-V} = 0.0005$ is applied following the law of Fitzpatrick (1999, with $R_V = 3.1$).

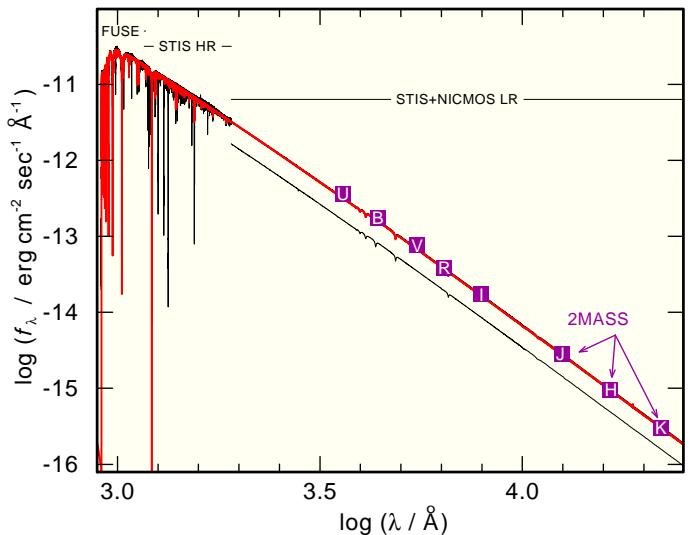


Fig. 4. Comparison of FUSE and HST (STIS and NICMOS) observations with our final model. A reddening of $E_{B-V} = 0.0005$ is applied. The low-resolution (LR) STIS+NICMOS observation vanishes behind the model SED due to the line width. Therefore, we plotted the observed spectrum twice, one shifted by $\Delta \log f_\lambda = -0.2$ for clarity. U, R, I (Landolt & Uomoto 2007), B, V (Høg et al. 2000), J, H, and K (Cutri et al. 2003) fluxes (converted from brightnesses using values given by Heber et al. 2002) are shown for comparison.

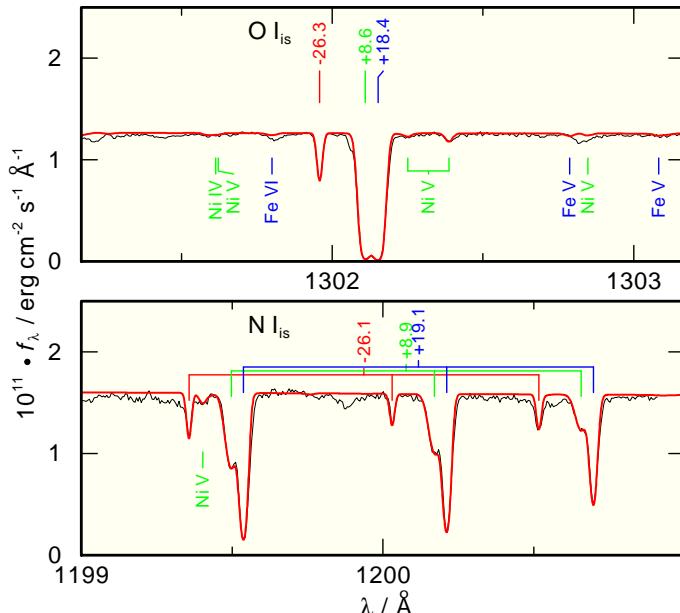


Fig. 3. STIS spectrum around the interstellar absorption lines $\text{O I} \lambda 1302.163 \text{\AA}$ (top) and $\text{N I} \lambda\lambda 1199.550, 1200.223, 1200.710 \text{\AA}$ (bottom) compared with the synthetic spectrum of our final model where the ISM lines are included. The labels give the radial velocities (in km/sec) that are applied.

$M = 0.555 M_\odot$ (Sect. 4.6) must have been ejected more than 500 000 years ago (Renedo et al. 2010). Its recombined, neutral gas, however, is still in the line of sight.

From the low interstellar N_{H_1} density, we expect a low interstellar reddening. The Galactic reddening law of Groenewegen & Lamers (1989), $\log(N_{\text{H}_1}/E_{B-V}) = 21.58 \pm 0.10$, predicts $0.0003 \lesssim E_{B-V} \lesssim 0.0007$. Figure 4 shows a comparison of observations and synthetic spectrum from the far UV (FUV) to the IR. We find $E_{B-V} = 0.0005 \pm 0.0005$.

3. Model atmospheres and atomic data

Table 2 demonstrates clearly that a panchromatic analysis from the EUV to the optical is inevitable for accurate results on photospheric parameters. Moreover, NLTE modeling is mandatory to calculate a reliable synthetic spectrum.

Lanz et al. (1996) presented the first NLTE model (Table 2) that reproduced the observed spectrum from the EUV to the optical wavelength range. Barstow & Hubeny (1998) introduced then a stratified H+He envelope including heavier metals in their models to improve the match to the observed flux below the He II absorption threshold ($\lambda \lesssim 228 \text{\AA}$). Later analyses had shown that there is further evidence for a stratification in G191–B2B’s photosphere. Vennes et al. (2000) closely examined Feige 24 that, compared with G191–B2B, has *similar atmospheric parameters and an almost identical abundance pattern*. They found that the $\text{O IV}/\text{O V}$ ionization equilibrium is overcorrected by -0.8 dex in their NLTE model. They concluded that this *might reveal an inhomogeneous vertical stratification of oxygen* in both stars. A later analysis of both stars (Vennes & Lanz 2001) showed that the average heavy-metal abundance in Feige 24 is 0.17 dex larger compared to the cooler and, hence, older G191–B2B (same $\log g$). Thus, the abundance pattern is determined by the same processes in both stars and the authors assumed that selective radiative pressure and gravity are in diffusive equilibrium. This was proven by Dreizler & Wolff (1999). They used self-consistent diffusion models (Table 2) that were able to reproduce the observed flux for $\lambda \lesssim 228 \text{\AA}$ without additional absorbers or mechanisms. However, problems remained with the fit to the UV lines.

Now, our strategy to proceed with the analysis is threefold. We start with chemically homogeneous models to find the model that reproduces best the continuum slope and the spectral lines from the FUV to the optical (Sect. 4). In an intermediate step, we will then apply the depth-dependent abundance profiles calculated by Dreizler & Wolff (1999) to our final homogeneous

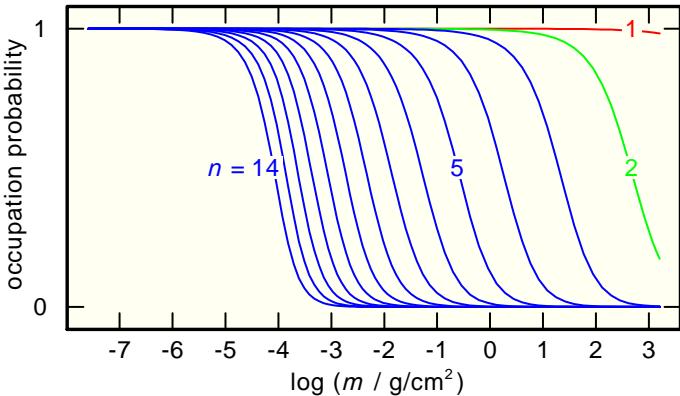


Fig. 5. Occupation probabilities of the H I levels with principal quantum numbers $n = 1 - 14$ in our final model.

model to investigate the impact of chemical stratification on the emergent spectrum (Sect. 4.3). In the last step, a diffusion model is calculated and compared with the homogeneous model (Sect. 4.4).

4. Spectral analysis and results

The metal-line blanketed NLTE model atmospheres for our analysis were calculated with the state-of-the-art Tübingen NLTE model-atmosphere package (Werner et al. 2003, TMAP⁶), which can consider opacities of all elements from H to Ni and beyond (Rauch 1997, 2003; Werner et al. 2012; Rauch et al. 2012). TMAP was successfully used for the spectral analysis of hot, compact stars (e.g. Rauch et al. 2007; Wassermann et al. 2010; Ziegler et al. 2012).

Our models assume plane-parallel geometry and are in hydrostatic and radiative equilibrium. Opacities of all species for which spectral lines are identified, namely H, He, C, N, O, Al, Si, P, S, Ca, Sc, Ti, V, Cr, Mn Fe, Co, Ni, Zn, Ge, and Sn, were considered in the model-atmosphere calculations. For all elements, we account for level dissolution (pressure ionization) following Hummer & Mihalas (1988) and Hubeny et al. (1994). Figure 5 demonstrates that our H I model ion (Tab. 4) includes all levels that are relevant in the line-forming region $-4.5 < \log[m/(g/cm^2)]$. All model atmospheres presented here cover column densities m of $-7.6 < \log m < 3.2$ (cf. Beuermann et al. 2006) represented by 90 depth points.

The model-atoms and respective absorption cross-sections for Ca – Ni were calculated via the recently registered VO service TIRO⁷ that uses Kurucz's atomic data⁸ and line lists (Kurucz 1991, 2009, 2011).

Ca, Sc, Ti, V, Cr, Mn, and Co lines are not identified. These were merged into a generic model atom (Rauch & Deetjen 2003) with fixed solar abundance ratios. Then, we performed test calculations and adjusted the abundance to a value (1.78×10^{-6} by mass, the solar value is 9.93×10^{-5}) where all of its lines just fade in the noise of the observed spectra. All other model atoms were constructed from data retrieved from the public Tübingen model-atom database TMAD⁹.

In total, we considered 1038 atomic levels in NLTE combined with 4646 line transitions (for the number of individual

iron-group lines, see Table 4) in the model-atmosphere calculations with 53 203 frequency points within $1 \times 10^{12} \text{ Hz} \leq \nu \leq 3 \times 10^{17} \text{ Hz}$. For the emergent spectra ($100 \text{ \AA} \leq \lambda \leq 400 000 \text{ \AA}$, 686 196 wavelength points), we account for fine-structure splitting and used 1585 NLTE levels and 9721 respective line transitions. The model-atom statistics are summarized in Tab. 4. Figure 6 shows the ionization fractions of all elements in our final model. It may be interesting to note that a single model atmosphere needs about one week to converge, i.e. the absolute values of all relative corrections are below 10^{-4} , on a 64 bit, 2.66 GHz compute core with 8 GB memory.

For the calculation of synthetic H I line profiles, we use Stark line-broadening tables provided by Tremblay & Bergeron (2009). For those lines, where no broadening tables are available, TMAP uses an approximate formula, as described in Ziegler et al. (2012, Eqs. 1 - 5).

We started with a model with $T_{\text{eff}} = 60 920 \text{ K}$ and $\log g = 7.55$ (the values of Gianninas et al. 2011) and the element abundances from Table 3. Next, we adjusted these abundances to best reproduce the respective spectral lines. We then calculated an extended grid of 234 model atmospheres ($48 000 \text{ K} \leq T_{\text{eff}} \leq 68 000 \text{ K}$ in steps of $\leq 1000 \text{ K}$ and $7.35 \leq \log g \leq 7.75$ in steps of 0.05 (some of the hotter models are calculated only for $\log g \leq 7.60$). For this grid, we extensively used compute resources of the bwGRiD¹⁰ in addition. Although this highly speeded up the model-grid calculation, the wide parameter range and the large number (15) of parameters to adjust simultaneously did not allow us to take a statistical approach in the spectral analysis (χ^2 method like e.g. in Gianninas et al. 2011) on a reasonable time scale. We therefore need to rely upon our “ χ -by-eye” methods. All SEDs that were calculated for this analysis are available via TheoSSA¹¹.

In a first analysis step, we will determine $\log g$ based on UV and optical observations. Then, we will determine T_{eff} precisely based on ionization equilibria of the metals which are sensitive indicators. Subsequently, we will adjust the abundances again and verify our T_{eff} and $\log g$ results.

4.1. Surface gravity and effective temperature

The dependency of the synthetic flux level on T_{eff} and $\log g$ for fixed abundances is demonstrated in Fig. 7, where we compare the observed and synthetic fluxes in the FUV. In the top panel, it is obvious that at a constant $T_{\text{eff}} = 60 920 \text{ K}$, a $\log g$ higher by 0.2 dex than $\log g = 7.55$ measured by Gianninas et al. (2011) is necessary to reproduce the Lyman-line decrement. For a fixed $\log g = 7.55$ (middle panel), a lower T_{eff} ($\Delta T_{\text{eff}} = 6000 \text{ K}$) improves the agreement between model and observation. The bottom panel shows that at values within the (statistical) error ranges from the H I Balmer-line analysis, $T_{\text{eff}} = 60 000 \text{ K}$ and $\log g = 7.60$ (cf. Table 2 Gianninas et al. 2011), a good agreement for both, line profiles and decrement, is achieved.

This was not expected from the outset although Barstow et al. (1998) found a relatively good agreement of T_{eff} and $\log g$ from H I Lyman and Balmer lines in the heavy-metal rich models (Table 2). The later analysis by Barstow et al. (2001, Table 2) shows strong deviations in $\log g$ between optical and FUV analyses. Figure 8 shows a comparison of synthetic H I Balmer line profiles with optical observations. The deviation between the $T_{\text{eff}} = 60 920 \text{ K} / \log g = 7.55$ and the $60 000 / 7.60$ ones is minor.

⁶ <http://astro.uni-tuebingen.de/~TMAP>

⁷ <http://astro.uni-tuebingen.de/~TIRO>

⁸ <http://kurucz.harvard.edu/atoms.html>

⁹ <http://astro.uni-tuebingen.de/~TMAD>

¹⁰ <http://www.bw-grid.de/en/the-bwgrid/>

¹¹ <http://dc.g-vo.org/theossa>

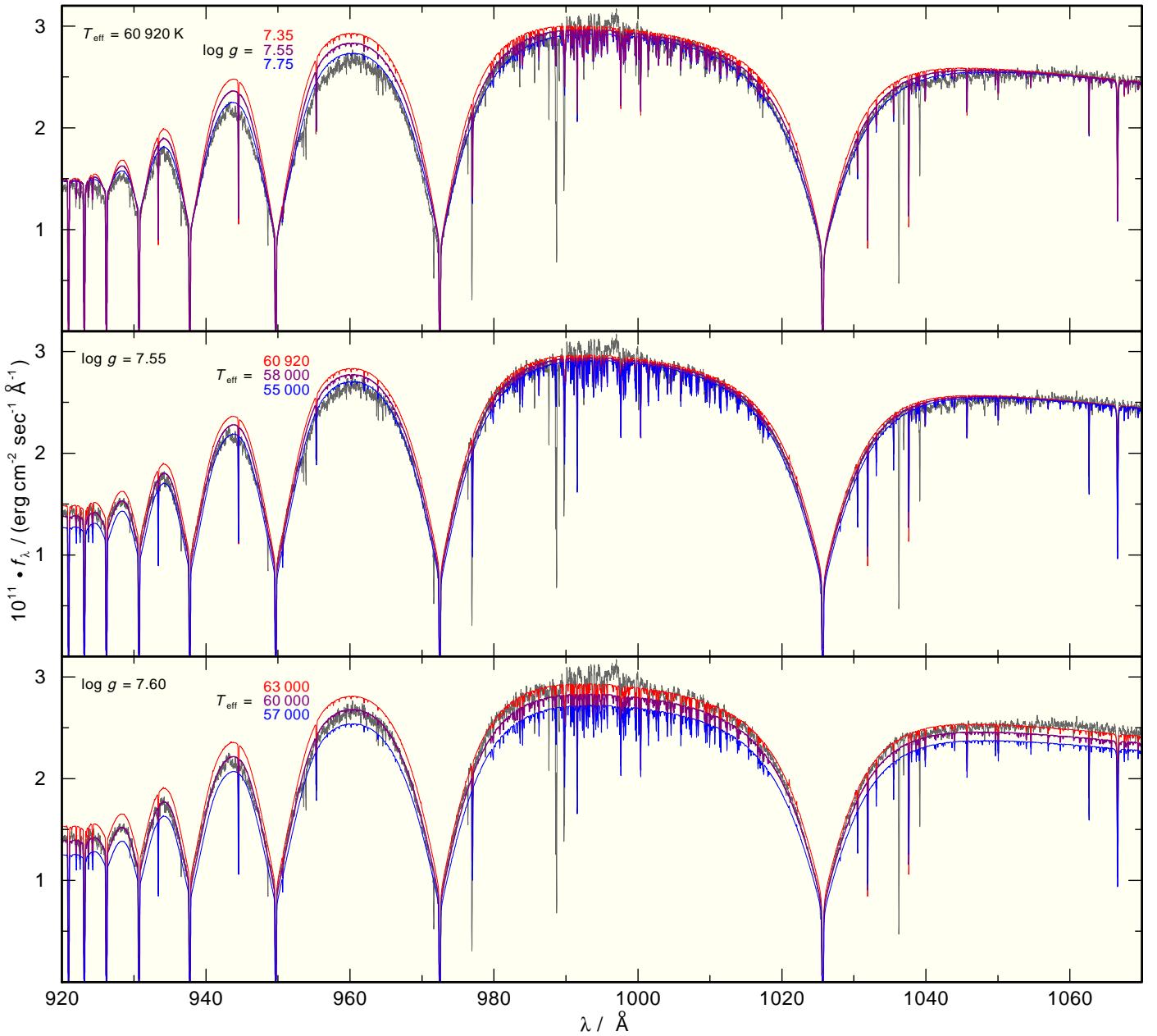


Fig. 7. Section of the FUSE observation compared with our model fluxes with different T_{eff} and $\log g$. In the top and middle panels, the synthetic fluxes are normalized to the observed flux at 1000 Å and in the bottom panel to the observed K magnitude (see Fig. 4). E_{B-V} and N_{H_1} are applied using our results from Sect. 2.3.

In addition to the low-resolution ($R \approx 500$) optical spectrum, medium-resolution ($R \approx 6000$) observations of H α and H β are shown in Fig. 9. The agreement among the STIS low and medium resolution is excellent. While the model absorption is a bit weak as shown in the lower plot of Fig. 9, the central NLTE emission reversal agrees well with the observations.

Although we cannot reproduce H α and H β in detail in the medium-resolution spectrum, this has no significant influence on our determination of T_{eff} and $\log g$ because the higher members of the H $_1$ Balmer series form much deeper in the atmosphere where the influence of metal opacities is less important (cf. Napiwotzki & Rauch 1994). We adopt $\log g = 7.60$.

In the next step of this analysis, we evaluate ionization equilibria of metals that exhibit lines of successive ionization stages. Figures 10, 11, and 12 show some strategic lines for this T_{eff}

determination. In total, we can use eight elements and lines of C $_{\text{III}} - \text{IV}$, N $_{\text{III}} - \text{V}$, Si $_{\text{III}} - \text{IV}$, P $_{\text{IV}} - \text{V}$, S $_{\text{IV}} - \text{V}$, Fe $_{\text{IV}} - \text{VI}$, Ni $_{\text{IV}} - \text{VI}$, and Ge $_{\text{IV}} - \text{V}$. $T_{\text{eff}} = 60\,000 \pm 2000$ K reproduces well all these equilibria simultaneously. For our further analysis, we adopt $T_{\text{eff}} = 60\,000$ K.

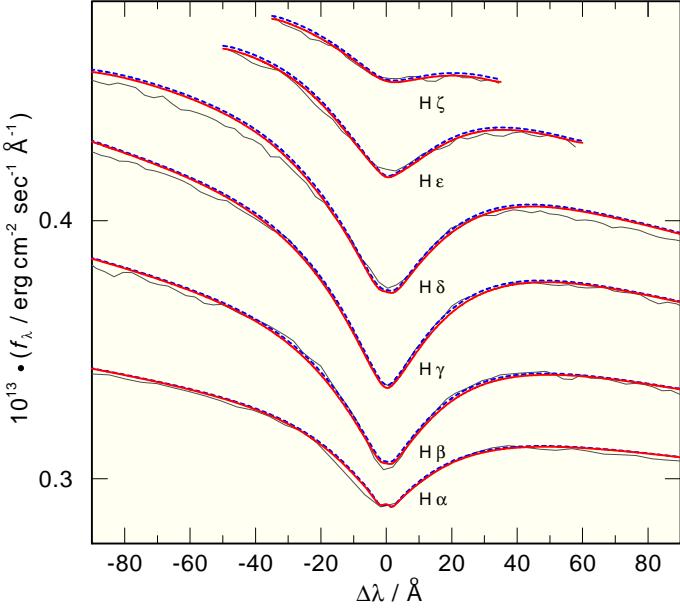


Fig. 8. Synthetic H I Balmer-line profiles compared with the STIS LR observation. The observation is shifted by factors of 0.921, 0.323, 0.232, 0.202, 0.193, and 0.188 for H α - H ζ , respectively, to fit into this plot. Red, full line: $T_{\text{eff}} = 60\,000$ K and $\log g = 7.60$; blue, dashed: $T_{\text{eff}} = 60\,920$ K and $\log g = 7.55$.

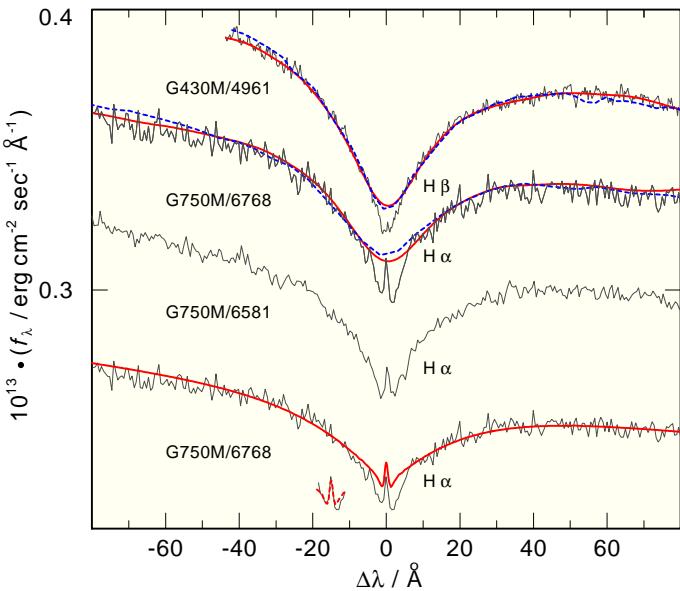


Fig. 9. STIS H α and H β low-resolution (dashed, blue) and medium-resolution (gray lines) observations (labeled with medium-resolution grating/central wavelength in Å). Because of uncertainty in the flux calibration, the medium-resolution data are normalized to the low-resolution flux. The flux around H β in the top plot is multiplied by a factor of 0.35. The red lines in the upper two plots are the medium-resolution ($R \approx 6000$) spectra degraded to the low resolution ($R \approx 500$) and agree with the low resolution (blue dash) within the uncertainty of the $R = 500$ resolution. The lower two plots are shifted down by 0.035 and 0.07×10^{-13} flux units, respectively. In the lowest plot, the model is overplotted in red after smoothing to the medium resolution. While the model H α absorption is somewhat too weak, the central emission agrees with the observation within the uncertainty of the resolution (inset).

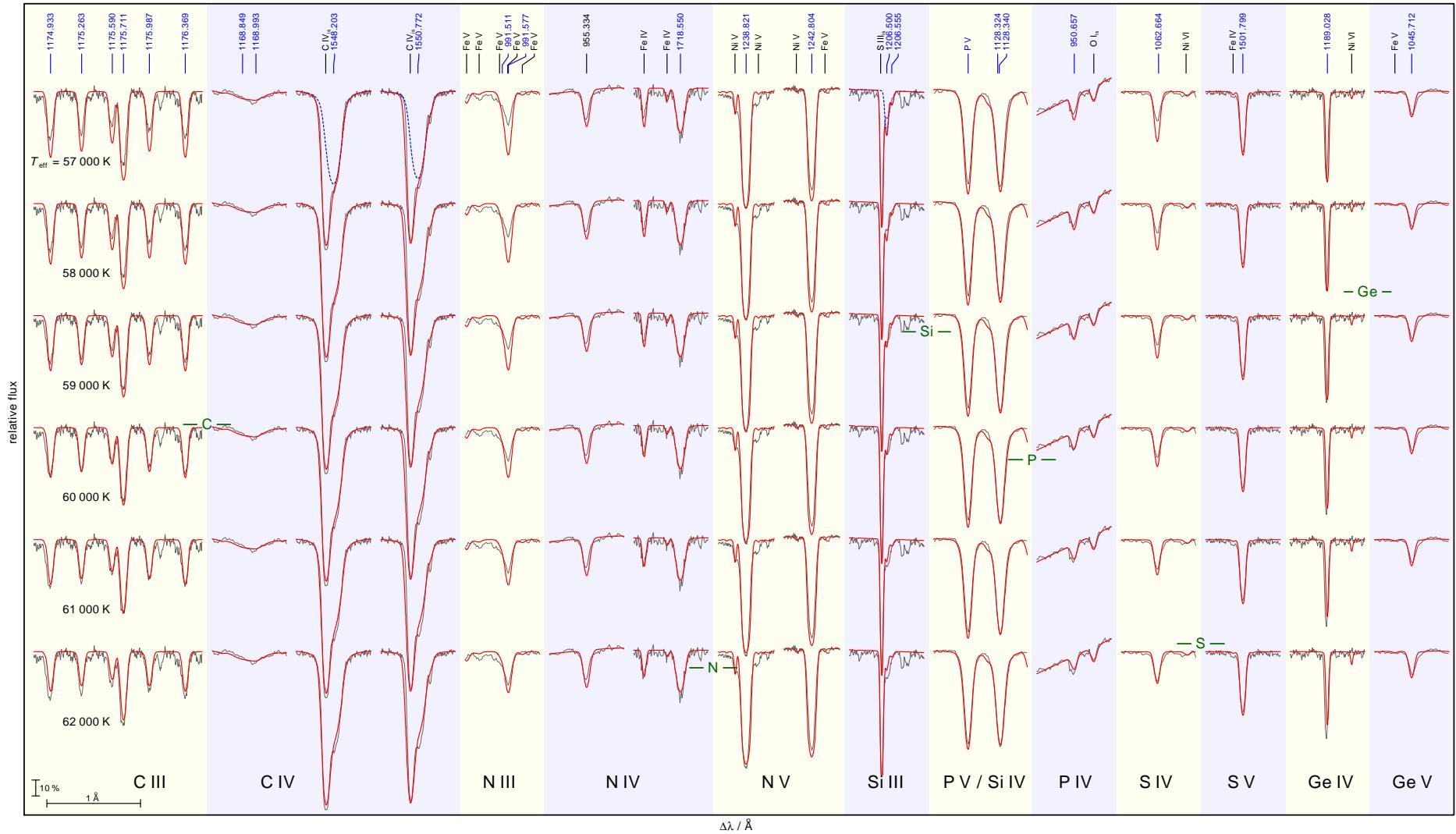


Fig. 10. Synthetic lines profiles of C III - iv, N III - v, Si III - iv, P IV - v, S IV - v, and Ge IV - v calculated from models with $57\,000\text{ K} \leq T_{\text{eff}} \leq 62\,000\text{ K}$ and $\log g = 7.6$ compared with FUSE and STIS observations. The small horizontal bars, labeled with the element's name, indicate T_{eff} where the ionization balance is best reproduced. The lines are identified at top. “is” denotes interstellar origin. In the cases of C IV $\lambda\lambda 1548, 1550\text{ \AA}$, C IV $\lambda\lambda 1548, 1550\text{ \AA}$, and Si III $\lambda\lambda 1206.500, 1206.555\text{ \AA}$, the photospheric line profile is shown by a dashed, blue line (for the $T_{\text{eff}} = 57\,000\text{ K}$ model at top only).

Table 6. Wavelengths (in Å) of unidentified strong ($W_\lambda > 10$ mÅ), likely photospheric lines in the FUSE and STIS observations.

FUSE				
989.11	1029.44	1133.04	1142.91	
STIS				
1157.60	1173.29	1183.82	1201.51	1283.52
1158.08	1174.34	1186.08	1201.81	1306.04
1158.76	1176.11	1186.27	1202.43	1331.19
1165.31	1176.52	1186.59	1204.47	1385.32
1166.80	1176.64	1187.70	1227.55	1389.89
1171.12	1176.87	1190.15	1253.67	1398.21
1171.19	1176.98	1192.01	1253.87	1411.46
1171.45	1177.06	1194.16	1258.81	1516.68
1172.18	1178.68	1198.15	1260.48	1520.64
1172.34	1182.00	1201.30	1272.98	1525.32
1173.22	1183.37	1201.47	1281.37	1538.94

4.2. Photospheric abundances

In the following, we use logarithmic mass fractions for all abundance values, if not otherwise mentioned. Previously determined abundances and respective references are summarized in Table 3. In the following, we will briefly mention the strategic lines for the abundance determinations and note abnormalities for an element selection only. Most of the identified metals exhibit lines of at least two subsequent ionization stages and some of these lines were already used for the determination of T_{eff} (Sect. 4.1). The abundances were then adjusted to achieve best line fits. Two large plots (German DIN A0 size) are provided in the online material that show a comparison of our final model with the observation in the FUSE and STIS wavelength ranges (in total 911 – 1750 Å). They include all line identifications (FUSE/STIS wavelength range), e.g. 2/421 Fe iv, 144/815 Fe v, 1/52 Fe vi, 1/236 Ni iv, 13/690 Ni v, and 9/43 Ni vi lines. These numbers are much higher than those of Preval et al. (2013, 106 Fe v and 44 Ni v lines in the STIS wavelength range). The recent work of Berengut et al. (2013) to employ G191–B2B as a stellar laboratory to determine the fine-structure constant is based on the latter list and may, thus, not fully exploit capacity of all the available STIS spectra of G191–B2B.

Our line identifications are also summarized in Table 5, whereas Table 6 gives a list of the strongest unidentified lines.

4.2.1. Helium

The first analyses revealed only upper limits for the He abundance, e.g. He < -3.1 and < 4.1 (Vennes et al. 1996; Gunderson et al. 2001, respectively). Cruddace et al. (2002) determined He = -4.2 ± 0.1 using high-resolution EUV spectroscopy. An attempt to identify and measure He ii Lyman lines ($n - n' = 1 - 4, 1 - 5$) with J-PEX¹² (Barstow et al. 2005) was not successful. Our models show that He ii $\lambda 1640$ Å (2 - 3) should be clearly visible at He = -3.7 and -4.2 and disappears in the noise of the observation only at about He < -4.7 (Fig. 13). We adopt this upper-limit value for our models.

4.2.2. Carbon, nitrogen, and oxygen

C III and C IV lines are visible in the observation. C III $\lambda 977.02$ Å and C IV $\lambda\lambda 1548.20, 1550.77$ Å have strong ISM blends. In case

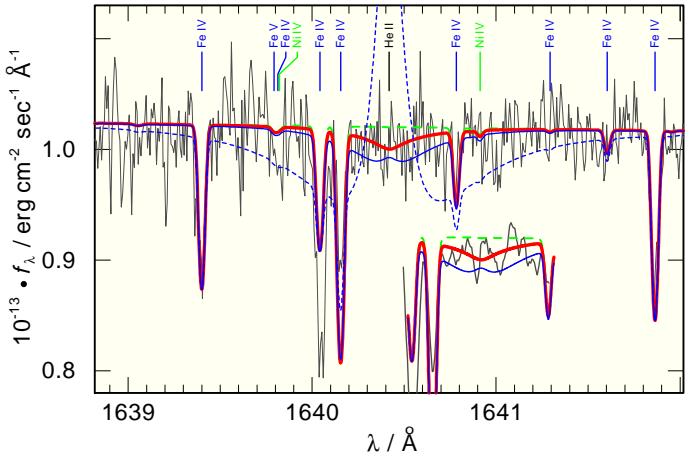


Fig. 13. Synthetic spectrum around He II $\lambda 1640.42$ Å compared with the STIS observation. the He abundances are green, dashed: -10.0, red, thick: -4.7, blue, thin: -4.2, blue, dashed: -3.1. The insert shows the region $\Delta\lambda = \pm 0.4$ Å around the He II line. For comparison, the observation was smoothed with a low-pass filter (Savitzky & Golay 1964, $n = 15$, $m = 4$).

of the latter, the photospheric component can be separated and modeled (Fig. 10). At C = -5.15, lines of both ions are well reproduced.

N III - v lines are found in the observation, they are all well matched at N = -5.58 (Fig. 10).

Vennes et al. (2000) encountered deviations between oxygen abundances determined from O IV and O V lines in an analysis of Feige 24. The O V abundance was 0.5 dex higher in their LTE model approach. In their NLTE models, they found that the O IV / O V ionization equilibrium was overcorrected by -0.8 dex. They suggested an inhomogeneous stratification of O in the atmosphere. Vennes & Lanz (2001) discovered that a similar problem exists in G191–B2B, with an overcorrection of -0.6 dex. Consequently they assumed that in both stars, the interplay between selective radiation pressure and gravity in diffusive equilibrium are the key processes for this phenomenon. Fig. 14 shows the same deviation in our models. While O IV $\lambda\lambda 1338.615, 1342.990, 1343.526$ Å are well fitted at O = -4.72, O V $\lambda 1371.296$ Å is apparently much stronger than observed. It is matched with an O abundance that is reduced by -0.4 dex.

In the FUSE observation, only the short wavelength component of the O VI $\lambda\lambda 1031.912, 1037.614$ Å resonance doublet is detectable. The unexpected weakness of this doublet was already reported by Oegerle et al. (2005). Dickinson et al. (2012b) verified that it stems from the photosphere. The O VI resonance doublet in our models is even stronger, compared to O IV and O V lines, requiring a reduction of the O abundance by about -1.5 dex (Fig 14). Dickinson et al. (2012a) encountered a similar problem with enigmatically deep line profiles of the N V resonance doublet in their models. We revisit the problem with the oxygen abundances derived from different ionization stages in Sections 4.3 and 4.4 in detail.

4.2.3. Aluminum, silicon, phosphorus, and sulfur

Holberg et al. (1998) identified the Al III $\lambda\lambda 1854.72, 1862.79$ Å resonance doublet in the IUE NEWSIPS SWP Echelle Data Set¹³, and Holberg et al. (2003) measured Al = -5.08. We could

¹² Joint Astrophysical Plasmodynamic Experiment

¹³ <http://vega.lpl.arizona.edu/newsips/>

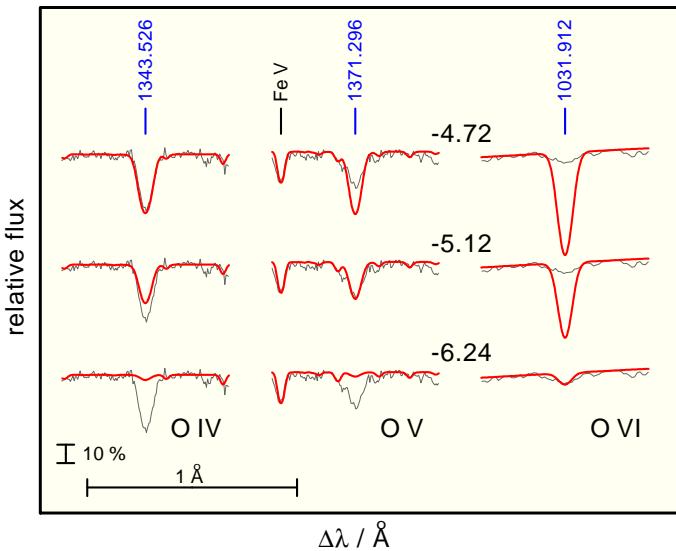


Fig. 14. The most prominent O_{IV}, O_V, and O_{VI} lines in the STIS and FUSE observations compared with our theoretical line profiles calculated with three O abundances (O = −4.72, −5.12, −6.24, from top to bottom).

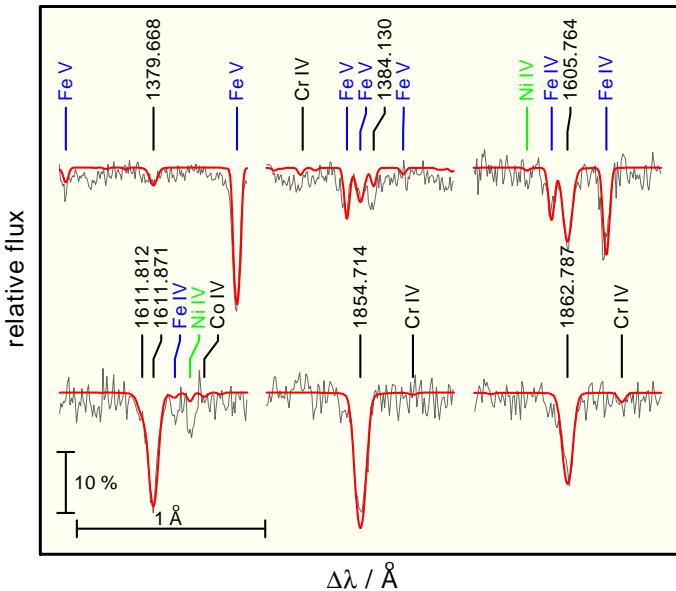


Fig. 15. Theoretical Al_{III} line profiles calculated from our final model compared with the STIS observation.

newly identify some other Al_{III} lines. We derive Al = −4.95, well in agreement with the Holberg et al. (2003) value (Fig. 15).

Si_{III} – iv, P_{IV} – v, and S_V – vi lines are identified. We determine Si = −4.30, P = −5.81, and S = −5.24 (Fig. 10).

4.2.4. Iron-group elements

Many hundreds of lines of Fe_{IV} – vi and Ni_{IV} – vi are identified (Table 5). They are best reproduced at Fe = −3.30 and Ni = −4.45. Note that the Ni/Fe abundance ratio is about 25 % higher than the solar ratio. Some of these lines are shown in various figures in this paper, please have a look at the two large online figures that show the complete FUSE and STIS wavelength ranges. An animation of STIS wavelength

range can be seen at http://astro.uni-tuebingen.de/~rauch/A0_E140H_SW.gif as well.

In Fig. 15 three lines of Cr_{IV} and one of Co_{IV} are visible in the synthetic spectrum of our final model. These are weak and comparable to the noise of the observation. Although one may be tempted to believe the presence of Cr_{IV} $\lambda\lambda$ 1863.075 Å, we take this as a hint that a log mass fraction of −5.75 for the generic model atom is reasonable and adopt this as an upper limit for our analysis. This is, within the error limits, in agreement with the upper limits for Cr, Mn, and Co of about −6.2 that was found by Holberg et al. (2003).

Preval et al. (2013) suggested that the unidentified line at 1272.98 Å is a V_{IV} line. Since many other V_{IV} lines with much stronger log *gf* values (*g* is the statistical weight of the lower atomic level and *f* is the oscillator strength of the line transition) from Kurucz's POS line lists (with good wavelengths) are not present in the spectrum, e.g. V_{IV} $\lambda\lambda$ 1355.127, 1419.577, 1426.647 Å (all more than ten times higher log *gf*) therefore this identification appears to be very unlikely.

We mention here that we find deviations between Kurucz's POS wavelengths and the observation of up to 0.05 Å. In addition, Fig. 13 shows that the strengths of Fe_{IV} $\lambda\lambda$ 1640.042 Å and Fe_{IV} $\lambda\lambda$ 1640.155 Å in the model are the opposite way around in the observation.

Figure 16 shows a comparison of models (calculated with Kurucz's POS lines) in the FUSE and STIS wavelength ranges where in each case the abundance of an individual element X in the construction of the generic (Ca, Sc, Ti, V, Cr, Mn, Co) model atom is increased by a factor of ten. Values higher than 1 in the flux ratio indicate stronger lines of element X.

E.g. the case of Ti, two lines are much stronger than all others, Ti_{IV} $\lambda\lambda$ 1451.739, 1467.343 Å. They are not identified in the observation but at the ten times increased abundance they are clearly visible in the model. The same is valid for Cr, where Cr_{IV} $\lambda\lambda$ 1332.415 Å and Cr_{VI} $\lambda\lambda$ 1417.660 Å are the strongest lines in our models (Fig. 16), and for Mn and Co as well. This allows us to establish upper abundance limits of about 10 % solar for Ti, Cr, Mn, and Co (cf. the beginning of Sect. 4).

4.2.5. Zinc, germanium, and tin

21 Zn_{IV} lines are newly identified in the STIS observation. These are almost all that are listed in the NIST¹⁴ database with relative intensities higher than 100. Since no individual calculations for Zn_{IV} transition probabilities are available, we adapted those of the isoelectronic Ge_{VI} (Rauch et al. 2012). In Fig. 17, we show nine of them with NIST relative intensities of 200. All their theoretical line profiles are reproduced at Zn = −4.89.

For Ge, we used the same model atom like Rauch et al. (2012) and determined Ge = −5.49 (Fig. 10).

We constructed a relatively small Sn model atom. The only lines for which reliable oscillator strengths are available are the Sn_{III} and Sn_{IV} resonance lines (Morton 2000). For all other allowed transitions, we follow Werner et al. (2012) and set *f* = 1. We used the Sn_{IV} λ 1314.537 Å resonance line, like Vennes et al. (2005), to measure the abundance of Sn = −6.45.

¹⁴ http://physics.nist.gov/PhysRefData/ASD/lines_form.html

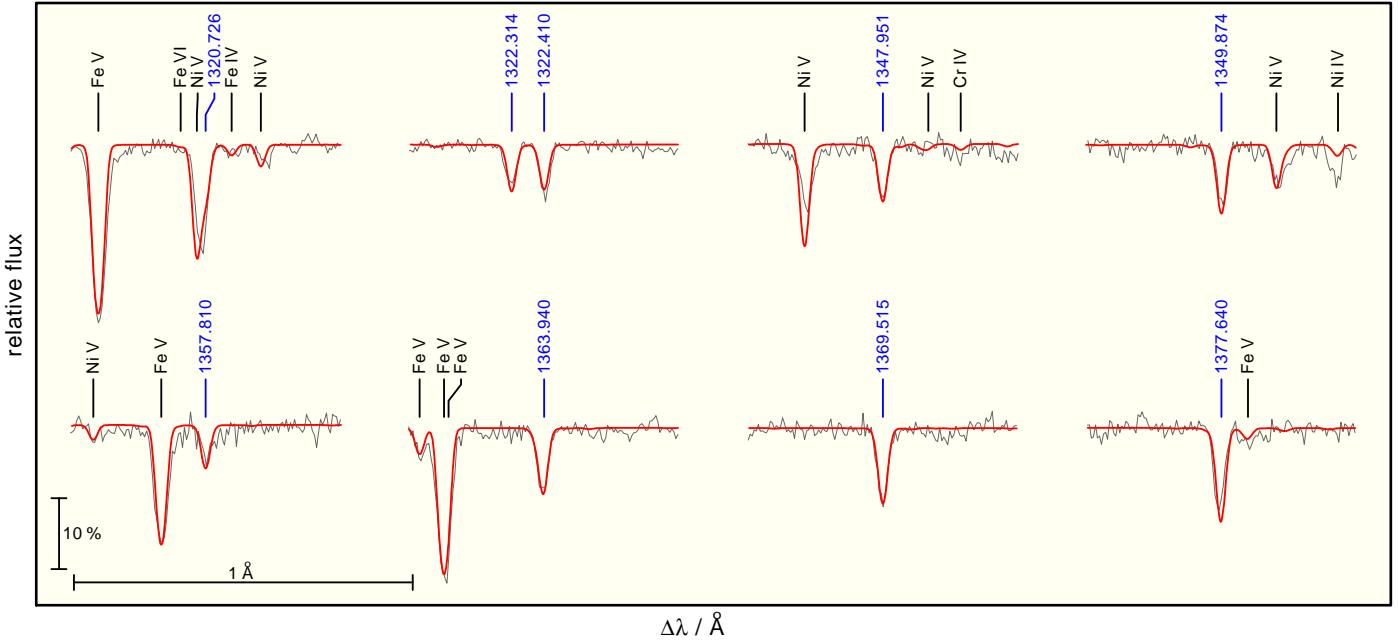


Fig. 17. Theoretical line profiles of the strongest Zn iv lines in the STIS wavelength range compared with the observation.

4.2.6. Summary of results with chemically homogeneous models

We can reproduce the entire ultraviolet spectrum of G191–B2B with our chemically homogeneous NLTE models, with the exception of the O iv / vi lines which are obviously affected by O stratification effects. Current diffusion models yield poor fits to the metal lines (Dreizler & Wolff 1999). $T_{\text{eff}} = 60\,000 \pm 2000$ K and $\log g = 7.60 \pm 0.05$ were determined within small error limits. They are in agreement with Gianninas et al. (2011, $T_{\text{eff}} = 60\,920 \pm 993$ K, $\log g = 7.55 \pm 0.05$). We do not encounter problems in modeling H I Lyman and Balmer lines simultaneously with the same T_{eff} and $\log g$ like found by Barstow et al. (2001, see Table 2).

We can determine all abundances with error limits of 0.2 dex. In case of Zn, where we adopt Ge vi f-values, we estimate that the error is 0.3 dex. Our C, N, O, Al, Si, Fe, and Ni abundances (Fig. 18) agree, within error limits, with those of Vennes et al. (1996); Holberg et al. (2003); Vennes et al. (2005). Our values are in general slightly higher. One reason may be the about 6000 K higher T_{eff} of our final model. The stellar parameters are summarized in Table 8.

The abundances of all elements but Fe predicted by Chayer et al. (1995) for a DA-type WD differ strongly from those that we determined (Fig. 18).

4.3. Test of the diffusion impact

In a first step, we simply applied the abundance profiles provided by Dreizler & Wolff (1999) to the occupation numbers of He, C, N, O, Si, and Ni in our final model. Figure 19 (top panel) shows that this gives a good agreement with O v while O iv is now too weak. The O vi lines appears even stronger, strengthening the discrepancy. Since the atmospheric structure was kept fixed in this test, we expected that, if at all, only a self-consistent diffusion model is able to reproduce the observed O iv - vi lines simultaneously.

4.4. A self-consistent diffusion model

We used the NGRT¹⁵ code (Dreizler & Wolff 1999; Schuh et al. 2002) to calculate diffusion models with the same element composition and model atoms like our homogeneous TMAP models. The first model shows a strongly increased abundance of the generic model atom that combines Ca, Sc, Ti, V, Cr, Mn, and Co (Sect.4) and, hence, much too strong lines of the considered elements. The reason is that the IrOnIc code (Rauch & Deetjen 2003) calculates a mean atomic weight for the generic atom following

$$A_{\text{IG}} = \frac{\sum_{i=1}^n r_i \cdot A_i}{\sum_{i=1}^n r_i}, \quad (1)$$

where r_i is the relative mass-fraction (with respect to $r_1 = 1$) and A_i the atomic weight of element i . The artificially increased number of lines of a single generic element strongly increases its radiative levitation. Flux blocking by the generic element then leads to stronger gravitational settling of other elements, e.g. Sn had an abundance below 10^{-17} throughout the model atmosphere. The other elements showed abundances that were partly more than one dex below those of our homogeneous model. Since we did not want to neglect all opacities of the generic atom, we changed its atomic weight to

$$A_{\text{IG}} = \sum_{i=1}^n r_i \cdot A_i. \quad (2)$$

Now, the stratified NGRT models yields depth dependent abundances (Fig. 20) that are closer to those of our homogeneous model, especially Sn appears at a realistic value. In case of He, C, N, O, Si, and Ni the abundance profiles are similar to those of (Dreizler & Wolff 1999). The changed atmospheric structure is shown in Fig. 21. It is interesting to note that most of the lines and all continua are formed at $\log m \gtrsim -3$ (Fig. 22)

¹⁵ New generation radiative transport

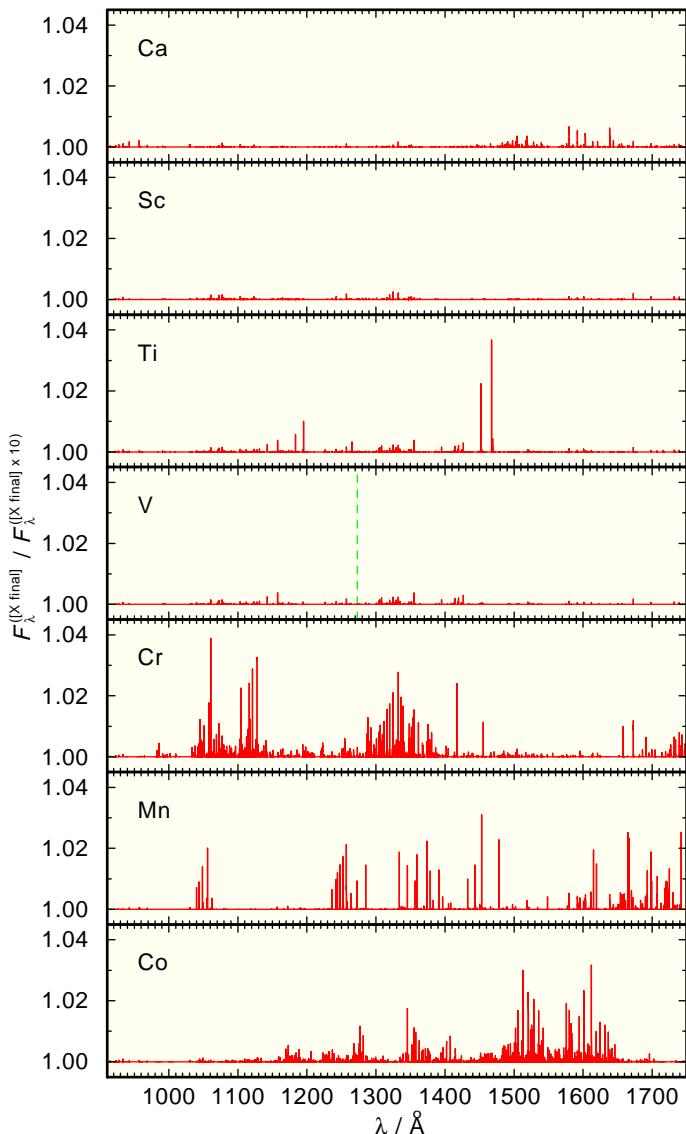


Fig. 16. Flux ratio of our final model and a model with ten times increased abundance of element X (Ca to Co, from top to bottom). The location of V_{IV} λ 1272.98 Å is marked.

while deviations in the temperature structure are noticeable only outside of this region. The resulting spectrum (Fig. 23) of the stratified model is, compared with the homogeneous model, no improvement. While Fe_v lines match the observation at about $T_{\text{eff}} = 55\,000$ K, it can be extrapolated that Fe_{iv} lines are much too strong for $T_{\text{eff}} \lesssim 70\,000$ K. Ni_{iv} and Ni_v lines are much too strong because the Ni abundance is enhanced (Fig. 20) in the line-forming regions and can, thus, not be used for a T_{eff} estimate.

In the stratified models, the O_{IV} and O_V lines are now much stronger than observed and O_{VI} appears at the same strength that resulted from our diffusion test (Sect. 4.3). The O abundance profile (Fig. 20) shows a strong increase for $\log m < -4$. Only by the introduction of an artificial abundance reduction by a factor of $m/1585$ for $\log m \lesssim -3.2$, we achieve an acceptable agreement of O_v and O_{vi} (Fig. 19). O_{IV} is still slightly too strong because the abundance and, thus, the lines (including a blend at O_{IV}) of the generic iron-group atom (Sect. 3) are overestimated by the NGRT model (Fig. 20). Based on this numerical exercise, it may be speculated that a weak stellar wind

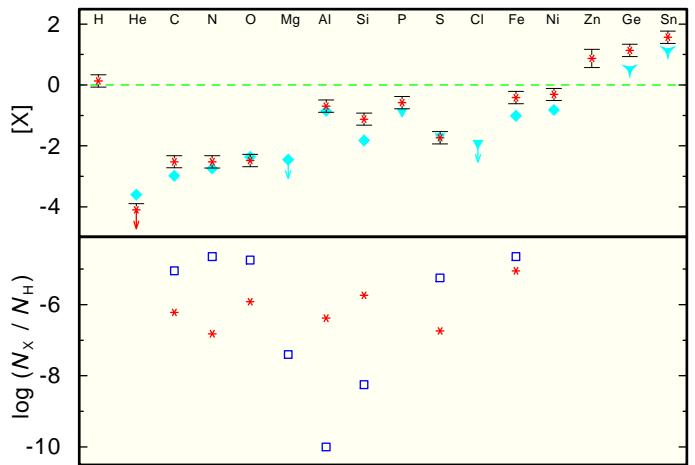


Fig. 18. Top: Photospheric abundances of G191–B2B (red stars) compared with solar values (Asplund et al. 2009). [X] denotes log (mass fraction / solar mass fraction) of element X. The dashed, green line shows the solar ratio. The arrows indicate upper limits. The cyan diamonds (Holberg et al. 2003), triangles (Vennes et al. 1996), and tridents (Vennes et al. 2005) are previously determined values. Bottom: Comparison of our abundance number ratios (red stars) with predictions of diffusion calculations for DA-type (blue squares) WDs (Chayer et al. 1995) with $T_{\text{eff}} = 60\,000$ K and $\log g = 7.5$.

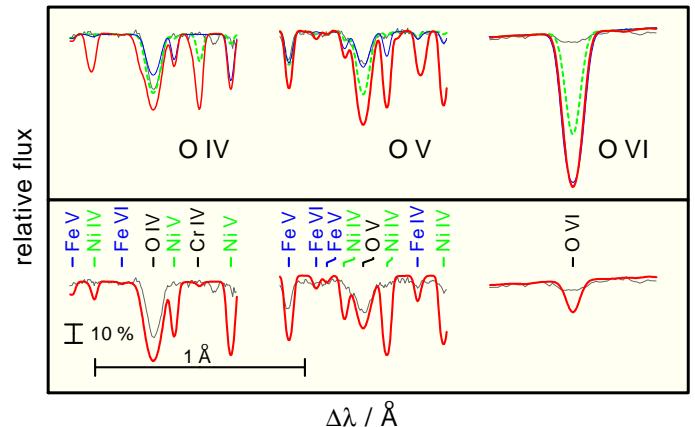


Fig. 19. Same as Fig. 14. Top: dashed, green TMAP (= chemically homogeneous) model with O = -4.72 ; thin, blue TMAP model with abundance profiles from Dreizler & Wolff (1999), thick, red NGRT (= diffusion) model. Bottom: thick, red NGRT model with an artificially reduced O abundance in the outer atmosphere. Note that in the NGRT models, the line strengths of the generic iron-group element (see text) are overestimated.

or an other, unknown process that is not considered by NGRT is responsible for the lower oxygen abundances in the outer atmosphere.

We can conclude two things. A generic model atom is obviously not suited for a diffusion calculation due to the strongly enhanced number of lines for a single atom in the modeling process. The NGRT diffusion models yield partly too low abundances in the line-forming regions and, thus, cannot reproduce the metal line properly. An additional, weak wind may be necessary to increase the metal abundances in the line-forming regions.

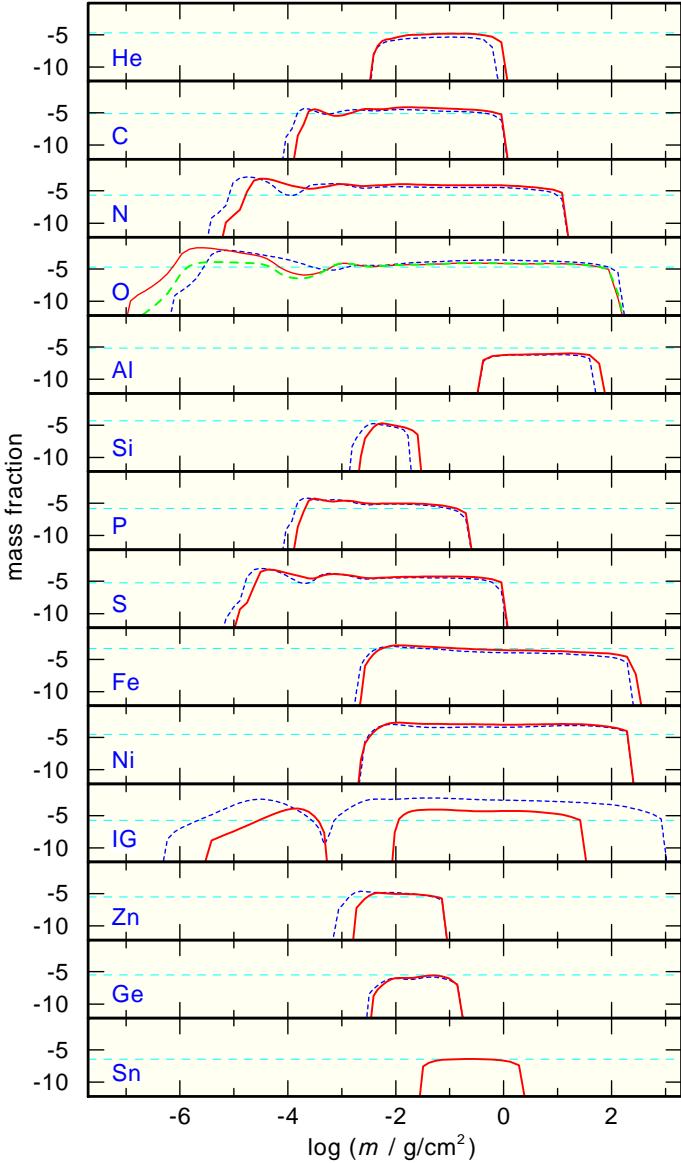


Fig. 20. Abundance profiles in our diffusion model ($T_{\text{eff}} = 60\,000$ K, $\log g = 7.60$). Short-dashed (blue) lines: unrealistically high abundance of the generic iron-group element (IG, see text), thick (red) lines: reduced IG abundance, horizontal long-dashed, thin (cyan) lines: the abundances in our final homogeneous model. In the O panel, the thick dashed (green) line shows our modified O-abundance profile (see text).

4.5. The extreme-ultraviolet spectrum

The inability to model the EUVE spectrum with chemically homogeneous atmospheres (Holberg et al. 1989) was the reason to investigate stratified photospheres (e.g. Koester 1991). Lanz et al. (1996) demonstrated, that it is possible to consistently match the optical, UV, and EUV data with homogeneous NLTE models with the same T_{eff} and chemical composition.

We calculated EUV spectra from our model grid with 193 584 frequency points within $100 \text{ \AA} \leq \lambda \leq 930 \text{ \AA}$, and Kurucz's LIN line lists (theoretical and laboratory measured lines, in total 8 135 405 lines of Ca - Ni in our wavelength interval, Kurucz 2009). These spectra were processed with the recently registered VO tool TEUV¹⁶ that corrects synthetic stellar fluxes for interstellar absorption below 911 Å. It simulates ra-

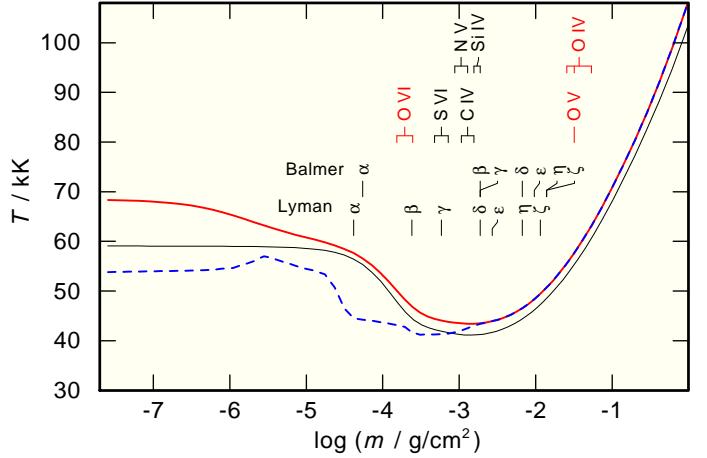


Fig. 21. Temperature structures ($T_{\text{eff}} = 60\,000$ K, $\log g = 7.60$) of a pure H model (thin, black), our final homogeneous model (thick, red), and a diffusion model (dashed, blue). The formation depths of the line cores of the lowest members of the H I Lyman and Balmer series, the C IV, N V, O VI, Si IV, and S VI resonance doublets, and our strategic O IV $\lambda\lambda 1338.634, 1343.022, 1343.526 \text{ \AA}$ and O V $\lambda 1371.296 \text{ \AA}$ lines are marked.

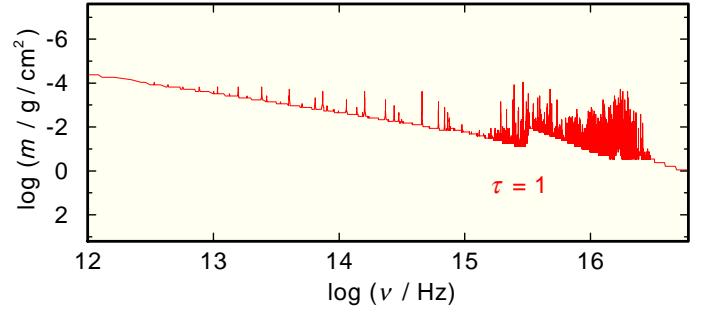


Fig. 22. Optical depth $\tau = 1$ in our final homogeneous model.

diative bound-free absorption of the lowest ionization states of H, He, C, N, and O using Opacity Project data (Seaton et al. 1994). Two interstellar components with different radial and turbulent velocities, temperatures, and column densities can be considered. Figure 24 shows the comparison of synthetic and observed EUV spectra. Our synthetic spectra were normalized to the measured FUSE flux of $1.347 \times 10^{-11} \text{ erg cm}^{-2} \text{ s}^{-1} \text{ \AA}^{-1}$ at 920 Å. Then, the interstellar column densities are adjusted, to match the EUVE flux $N_{\text{H}\,\text{I}}$ for 530 Å, $N_{\text{He}\,\text{I}}$ for 470 Å, and $N_{\text{He}\,\text{II}}$ for 220 Å. Since our models do not reproduce the measured flux between 250 Å and the He II ground state threshold, $N_{\text{He}\,\text{II}}$ is not reliable. Table 7 shows the applied $N_{\text{H}\,\text{I}}$ and $N_{\text{He}\,\text{I}}$ values compared with the literature values. Our $N_{\text{H}\,\text{I}}$ values, necessary to match the EUVE flux level, are about a factor of two higher than $\log(N_{\text{H}\,\text{I}} / \text{cm}^2) = 18.34^{+0.08}_{-0.10}$ that we determined previously from H I Lyman-line fits (Sect. 2.3). $\log N_{\text{N}\,\text{I}} = 13.87$ and $\log N_{\text{O}\,\text{I}} = 14.86$ were adopted from Lemoine et al. (2002).

The overall agreement of our homogeneous models with $T_{\text{eff}} = 60\,000$ K at wavelengths $\lambda \gtrsim 250 \text{ \AA}$ is very good, especially the interval $360 \text{ \AA} \lesssim \lambda \lesssim 450 \text{ \AA}$ is excellently matched in detail. Models with $T_{\text{eff}} = 65\,000$ K and $T_{\text{eff}} = 55\,000$ K yield much too high and too low fluxes, respectively. At $\lambda \lesssim 250 \text{ \AA}$ the theoretical flux is too high in all models, even at $T_{\text{eff}} = 55\,000$ K. A stratified model (Fig. 24) with $T_{\text{eff}} = 60\,000$ K fails to reproduce the flux between $250 \text{ \AA} \lesssim \lambda \lesssim 420 \text{ \AA}$ and has a too-high flux at $\lambda \lesssim 200 \text{ \AA}$.

¹⁶ <http://astro.uni-tuebingen.de/~TEUV>

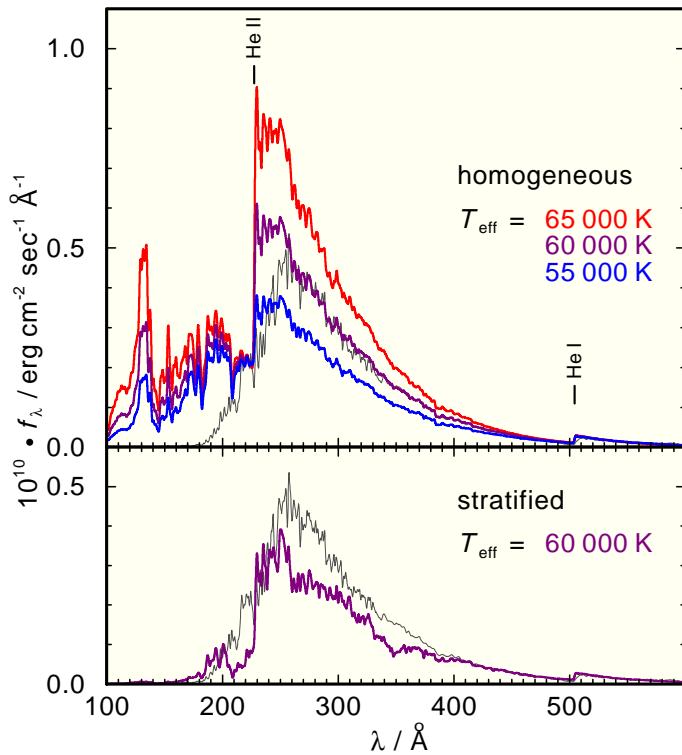


Fig. 24. Top: Comparison of three synthetic spectra ($T_{\text{eff}} = 55\,000$, $60\,000$, and $65\,000$ K) of chemically homogeneous models with the EUVE observation. The wavelengths of ground-state absorption thresholds of He ions are indicated. Bottom: Comparison of a stratified model $T_{\text{eff}} = 60\,000$ K with the observation.

Table 7. Logarithmic ISM column densities for homogeneous models with different T_{eff} to match the EUVE flux level of G191–B2B.

$T_{\text{eff}} / \text{K}$	N_{H_1}	N_{He_1}	
homogeneous (TMAP)			
55 000	18.53	17.45	
60 000	18.59	17.45	
65 000	18.64	17.45	
stratified (NGRT)			
60 000	18.60	17.45	
literature			
59 250	18.23	17.16	Kimble et al. (1993, HUT)
54 000	18.27	17.16	Dupuis et al. (1995, EUVE)
55 200	18.32	17.26	Lanz et al. (1996, EUVE)
56 000	18.32	17.15	Dreizler & Wolff (1999, EUVE)
53 000	18.28	17.16	Vennes & Lanz (2001, EUVE)
54 000	18.33	17.34	Cruddace et al. (2002, J-PEX)

Both, our homogeneous and our stratified models, fail to reproduce the entire EUV spectrum of G191–B2B. It seems likely that there may be some stratification in the atmosphere but we don't yet know how to distribute the various atomic species with depth. This is a challenge for theorists.

4.6. Mass and distance

A stellar mass of $M = 0.555^{+0.035}_{-0.029} M_{\odot}$ and a luminosity of $\log(L/L_{\odot}) = 0.63^{+0.37}_{-0.34}$ are determined by comparison with evolutionary models (Fig. 25) for old white dwarfs (metallicity $z = 0.001$).

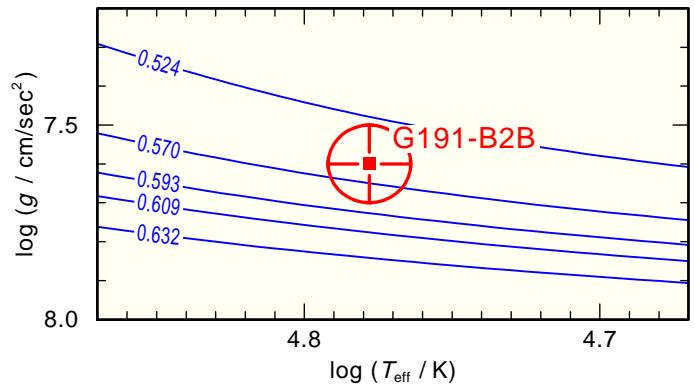


Fig. 25. Location of G191–B2B in the $\log T_{\text{eff}} - \log g$ plane (the ellipse indicates the errors of our analysis) compared with evolutionary tracks for hydrogen-rich white dwarfs (Renado et al. 2010) labeled with the respective stellar masses (in M_{\odot}).

Table 8. Parameters of G191–B2B as derived by our analysis.

$T_{\text{eff}} / \text{K}$	$60\,000 \pm 2000$		
$\log(g / \text{cm/sec}^2)$	7.60 ± 0.05		
element	mass fraction	number	[X]
H	9.99×10^{-1}	1.0	0.132
He	$< 1.98 \times 10^{-5}$	$< 5.0 \times 10^{-6}$	< -4.099
C	7.15×10^{-6}	6.0×10^{-7}	-2.520
N	2.08×10^{-6}	1.5×10^{-7}	-2.522
O	1.90×10^{-5}	1.2×10^{-6}	-2.479
Al	1.12×10^{-5}	4.2×10^{-7}	-0.695
Si	5.01×10^{-5}	1.8×10^{-6}	-1.123
P	1.54×10^{-6}	5.0×10^{-8}	-0.579
S	5.72×10^{-6}	1.8×10^{-7}	-1.733
Ti	$< 3.13 \times 10^{-7}$	$< 1.1 \times 10^{-7}$	< -0.100
Cr	$< 1.66 \times 10^{-6}$	$< 5.1 \times 10^{-7}$	< -0.100
Mn	$< 1.08 \times 10^{-6}$	$< 3.2 \times 10^{-7}$	< -0.100
Fe	4.98×10^{-4}	9.0×10^{-6}	-0.414
Co	$< 4.92 \times 10^{-7}$	$< 1.2 \times 10^{-7}$	< -0.100
Ni	3.49×10^{-5}	6.0×10^{-7}	-0.310
Zn	1.30×10^{-5}	2.0×10^{-7}	0.873
Ge	3.24×10^{-6}	4.5×10^{-8}	1.135
Sn	3.53×10^{-7}	3.0×10^{-9}	1.569
E_{B-V}	0.0005 ± 0.0005		
$\log(N_{\text{H}_1} / \text{cm}^2)$	$18.34^{+0.08}_{-0.10}$		
$\log(N_{\text{D}_1} / \text{cm}^2)$	$13.54^{+0.05}_{-0.06}$		
d / pc	62 ± 4		
M / M_{\odot}	$0.555^{+0.035}_{-0.029}$		
R / R_{\odot}	$0.0195^{+0.0004}_{-0.0005}$		
$\log(L / L_{\odot})$	$0.63^{+0.37}_{-0.34}$		

We calculated the spectroscopic distance following the flux calibration of Heber et al. (1984b) for $\lambda_{\text{eff}} = 5454$ Å,

$$d[\text{pc}] = 7.11 \times 10^{-4} \cdot \sqrt{H_v \cdot M \cdot 10^{0.4m_{v_0} - \log g}}, \quad (3)$$

with $m_{v_0} = m_v - 2.175c$, $c = 1.47E_{B-V}$, and the Eddington flux $H_v = 1.109 \times 10^{-3} \text{ erg cm}^{-2} \text{ s}^{-1} \text{ Hz}^{-1}$ at λ_{eff} of our final model atmosphere. We used $E_{B-V} = 0.0005 \pm 0.0005$ (Sect. 2.3),

$M = 0.555^{+0.035}_{-0.029} M_{\odot}$, and $m_V = 11.7228 \pm 0.0082$ (van Leeuwen 2007), and derived a distance of $d = 62 \pm 4$ pc and a height above the Galactic plane of $z = 8 \pm 1$ pc. This is in agreement with the HIPPARCOS¹⁷ parallax measurement (van Leeuwen 2007, HIP23692) of $d = 59.88^{+9.05}_{-12.95}$ pc and the XHIP¹⁸ value of $d = 57.96 \pm 10.31$ pc (Anderson & Francis 2012). The spectroscopic distance of $d = 55.84 \pm 0.86$ pc determined by Holberg et al. (2008) is slightly smaller, this error estimate, however, appears to be too optimistic.

5. TheoSSA: synthetic stellar spectra on demand

At the end, we want to compare our final TMAP model flux with an SED, that was calculated with the TMAW tool (Sect. 1) and considers H, He, C, N, and O only. Figure 26 shows that the TMAP flux is higher everywhere at $\lambda > 911$ Å. The reason is strong metal-line blanketing at $\lambda < 911$ Å that causes a flux increase at longer wavelengths. It amounts to about 10 % at 1000 Å and to about 5 % at 7000 Å. The lower panel of Fig. 26 illustrates that the theoretical line profiles of the H I Balmer series are almost identical in both, TMAP and TMAW models, with the exception of an increased emission reversal in the line core of H α in the TMAP model.

The TheoSSA database contains currently TMAP SEDs of a dozen standard stars. Some of them are represented by different models for comparison, because they were initially calculated for the calibration (Vernet et al. 2008a,b, 2010) of ESO's¹⁹ second generation VLT²⁰ instrument XSHOOTER²¹ (Vernet et al. 2011) while the parameters of Gianninas et al. (2011) and Giannicchele et al. (2012) were published later (Table 9).

6. Accuracy of flux calibration with G191–B2B

Our spectral analysis was performed using state-of-the-art atomic data and model-atmosphere code. The best reproduction of UV and optical spectra was achieved with chemically homogeneous models. In Fig. 27, we compared two models at the edge of our error ranges in T_{eff} and $\log g$. The deviation in the continuum flux of two TMAP model SEDs is ≈ 3 % in the optical and ≈ 5 % in the FUV. A systematic error is present due to the uncertainty of the used atomic data, such as oscillator strengths where it is typically ≈ 15 % for a single line. The employment of many lines of many ions of many atoms in a spectral analysis minimizes the propagation of these uncertainties into the errors of the main photospheric properties like T_{eff} , $\log g$, and the abundances. An additional systematic error may be present between individual model-atmosphere packages (e.g. Rauch 2008b) because of differences in coding, approximations, etc.

The situation for the flux calibration is, however, not that strongly dependent on the exact T_{eff} and $\log g$ values (the latter is even less important). E.g. in the case of G191–B2B and our errors (3 % in T_{eff} and 0.05 dex in $\log g$), a normalization to a precisely measured brightness will reduce the deviation between model SED and observation much below 1 % in the optical and infrared. The residuals among the three primary stars G191–B2B, GD 71, and GD 153 are generally sub percent at the longer wavelengths (Bohlin 2007) The remaining deviation in

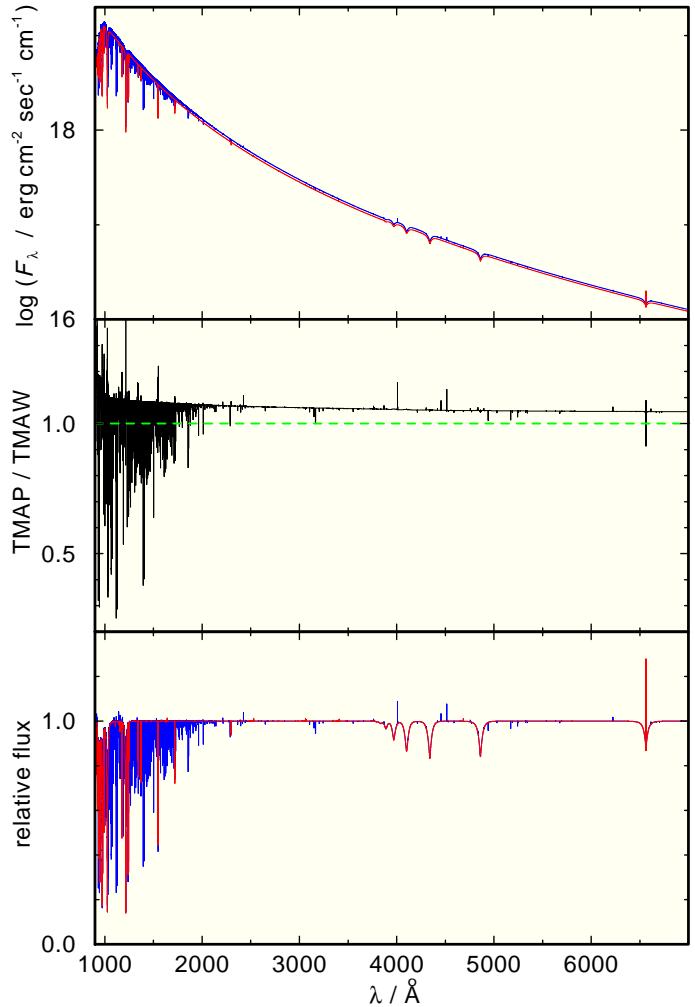


Fig. 26. Comparison of our final TMAP model (blue, thick) with a TMAW model (red, thin). Top: astrophysical fluxes at the stellar surface, middle: ratio TMAP/TMAW flux, bottom: normalized fluxes.

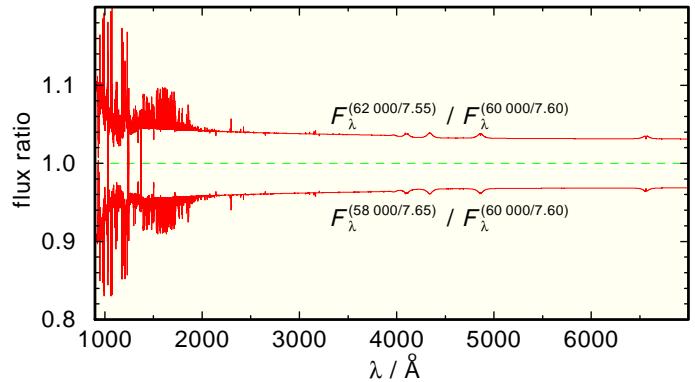


Fig. 27. Flux ratio of two TMAP models at the edge of the T_{eff} and $\log g$ error ranges and our final model.

the FUV wavelength range is presently less than 2 %. Further improvement is essentially dependent on the reliability of the atomic data (Sect. 7).

7. Conclusions

The TheoSSA service is designed to provide theoretical stellar SEDs of any kind in VO-compliant form. Its efficiency is

¹⁷ <http://www.rssd.esa.int/index.php?project=HIPPARCOS>

¹⁸ Extended HIPPARCOS compilation

¹⁹ European Southern Observatory

²⁰ Very Large Telescope

²¹ <http://www.eso.org/sci/facilities/paranal/instruments/xshooter>

Table 9. Standard star SEDs (references for T_{eff} and $\log g$ are given) presently available in TheoSSA. WD numbers are from McCook & Sion (1999).

name	WD no.	spectral type	T_{eff} [K]	$\log g$ [cm/sec 2]
EG 274	1620–391	DA2 (+ G5V)	24 276	8.01 ^a
			25 980	7.96 ^{b, c}
Feige 67		Op+WDsd	75 000	5.20 ^d
			40 000	5.00 ^e
Feige 110	2317–054	sdO	58 883	7.46 ^a
			61 193	7.49 ^f
G191–B2B	0501+527	DA0	60 920	7.55 ^b
			60 000	7.55 ^g
G 93–48	2149+021	DAZ3	18 100	7.85 ^h
			18 170	8.01 ^b
GD 50	0346–011	DA2	40 550	9.22 ⁱ
			42 700	9.20 ^b
GD 71	0549+158	DA1	32 747	7.68 ^f
			32 780	7.83 ⁱ
			33 590	7.93 ^b
GD 108	0958–073	sdB	22 908	5.30 ^j
GD 153	1254+223	DA1.5	38 205	7.89 ⁱ
			38 686	7.66 ^f
			40 590	7.93 ^b
HZ 2	0410+117	DA3	20 600	7.90 ^h
			21 600	7.98 ^b
HZ 43A	1314+293	DA1+dM3e	51 116	7.90 ^k
			56 800	7.89 ^b
Sirius B	0642–166	DA2	24 826	8.60 ^k
			25 970	8.57 ^{b, c}

Notes.

- (^a) assumed
- (^b) Gianninas et al. (2011)
- (^c) Giammichele et al. (2012)
- (^d) Bauer & Husfeld (1995)
- (^e) Heber et al. (1984a), He mass fraction of 0.107
- (^f) Finley et al. (1997)
- (^g) this work
- (^h) Guseinov et al. (1983)
- (ⁱ) Barstow et al. (2001)
- (^j) Kilkenny et al. (1988)
- (^k) Beuermann et al. (2006)

strongly increasing if more different model-atmosphere groups provide their SEDs with a proper description in their respective meta data. The establishment of a database of spectrophotometric standard stars is an opportunity to use the same model SEDs for astrophysical flux calibration. Many model-atmosphere groups have their own best models for some of these stars, for which a common base for comparison arises. Differences in the algorithms for considered physics, assumptions, and approximations in different model-atmosphere codes, lead to systematic deviations in general.

Figure 28 shows the temporal development of the T_{eff} and $\log g$ determinations of G191–B2B. While both values had a large scatter in the 1990s (error ranges are not shown for clarity), the three most recent analyses, that are all based on sophisticated NLTE model-atmosphere techniques, show a good agreement within relatively narrow error ranges of about 3 % in T_{eff} and 0.05 dex ($\approx 12\%$) in $\log g$. Ironically, these latest results agree quite well with the very first line-profile analysis presented by Holberg et al. (1986) performed with a Ly α line-profile fit with a simple, pure-H LTE model atmosphere. The TheoSSA database may help to get closer to the intended goal of 1 % accuracy in absolute flux calibration.

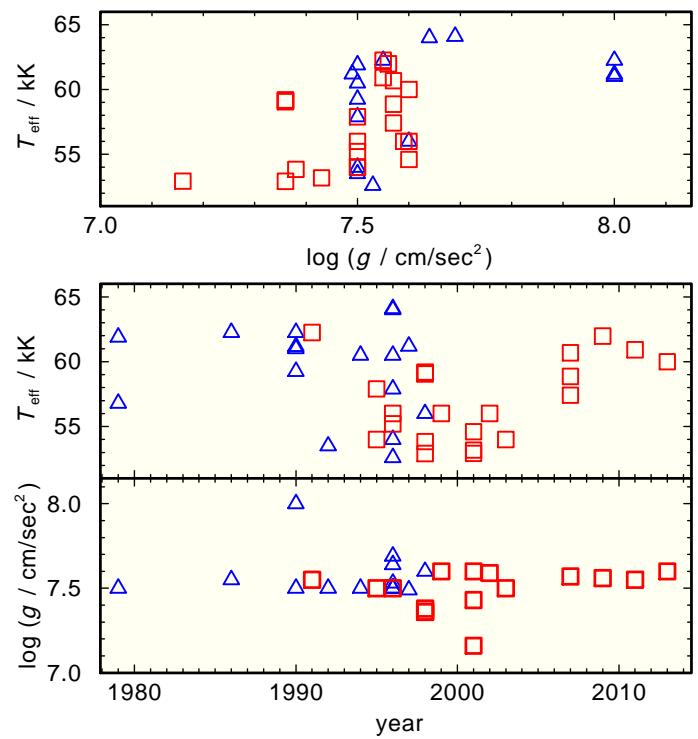


Fig. 28. Determined T_{eff} and $\log g$ values in the last 34 years. Blue triangles denote analyses with LTE models, red squares those with NLTE models (Table 2). The result of Koester et al. (1979, $\log g = 5.95$) is outside the top and bottom panels.

We presented here our spectral analysis of G191–B2B to demonstrate the current state-of-the-art. We are presently able to reproduce the observed spectrum from 250 Å to the infrared. The EUV part from 150 Å to 250 Å cannot be modeled, neither by our homogeneous nor by our stratified models. The reason is unknown.

A similar analysis of the UV spectrum of the calibration star BD +28°4211 ($T_{\text{eff}} = 82\,000 \pm 5\,000$ K, $\log g = 6.2^{+0.3}_{-0.1}$) was just published by Latour et al. (2013).

Model-atmosphere codes have arrived now at a high level of sophistication, and we already encounter problems getting reliable atomic data to reproduce the high-resolution and high-S/N spectra that are obtained with presently available instruments. This is a challenge for atomic physicists to be prepared for upcoming telescopes and instruments.

Acknowledgements. TR is supported by the German Aerospace Center (DLR, grant 05 OR 1301). The GAVO project at Tübingen has been supported by the Federal Ministry of Education and Research (BMBF, grants 05 AC 6 VTB, 05 AC 11 VTB). AstroGrid-D was funded by the BMBF (01 AK 804 [A-G]). The bwGRid²² is funded within the framework of the D-Grid Project by the BMBF. This research has made use of the SIMBAD database, operated at CDS, Strasbourg, France. This research has made use of NASA's Astrophysics Data System. This work used the WRPLOT visualization software developed by Wolf-Rainer Hamann (Potsdam) and the WRPLOT team. Some of the data presented in this paper were obtained from the Mikulski Archive for Space Telescopes (MAST). STScI is operated by the Association of Universities for Research in Astronomy, Inc., under NASA contract NAS5-26555. Support for MAST for non-HST data is provided by the NASA Office of Space Science via grant NNX09AF08G and by other grants and contracts. The TEUV tool (<http://astro-uni-tuebingen.de/~TEUV>) used to apply interstellar corrections to theoretical spectra was constructed as part of the activities of the German Astrophysical Virtual Observatory. The TIRO service (<http://astro-uni-tuebingen.de/~TIRO>) used to calculate opacities for this pa-

²² <http://www.bw-grid.de/en/the-bwgrid/>

per was constructed as part of the activities of the German Astrophysical Virtual Observatory.

References

- Allende Prieto, C., Hubeny, I., & Smith, J. A. 2009, MNRAS, 396, 759
- Anderson, E. & Francis, C. 2012, Astronomy Letters, 38, 331
- Asplund, M., Grevesse, N., Sauval, A. J., & Scott, P. 2009, ARA&A, 47, 481
- Barstow, M. A., Crudde, R. G., Kowalski, M. P., et al. 2005, MNRAS, 362, 1273
- Barstow, M. A., Good, S. A., Holberg, J. B., et al. 2003, MNRAS, 341, 870
- Barstow, M. A., Holberg, J. B., Hubeny, I., et al. 2001, MNRAS, 328, 211
- Barstow, M. A. & Hubeny, I. 1998, MNRAS, 299, 379
- Barstow, M. A., Hubeny, I., & Holberg, J. B. 1998, MNRAS, 299, 520
- Bauer, F. & Husfeld, D. 1995, A&A, 300, 481
- Berengut, J. C., Flambaum, V. V., Ong, A., et al. 2013, Physical Review Letters, 111, 010801
- Beuermann, K., Burwitz, V., & Rauch, T. 2006, A&A, 458, 541
- Beuermann, K., Burwitz, V., & Rauch, T. 2008, A&A, 481, 769
- Bohlin, R. C. 2007, in Astronomical Society of the Pacific Conference Series, Vol. 364, The Future of Photometric, Spectrophotometric and Polarimetric Standardization, ed. C. Sterken, 315
- Bohlin, R. C., Dickinson, M. E., & Calzetti, D. 2001, AJ, 122, 2118
- Chayer, P., Fontaine, G., & Wesemael, F. 1995, ApJS, 99, 189
- Chayer, P., Vennes, S., Pradhan, A. K., et al. 1996, in IAU Colloq. 152: Astrophysics in the Extreme Ultraviolet, ed. S. Bowyer & R. F. Malina, 211
- Crudde, R. G., Kowalski, M. P., Yentis, D., et al. 2002, ApJ, 565, L47
- Cutri, R. M., Skrutskie, M. F., van Dyk, S., et al. 2003, VizieR Online Data Catalog, 2246, 0
- Dickinson, N. J., Barstow, M. A., & Hubeny, I. 2012a, MNRAS, 421, 3222
- Dickinson, N. J., Barstow, M. A., Welsh, B. Y., et al. 2012b, MNRAS, 423, 1397
- Dreizler, S. & Wolff, B. 1999, A&A, 348, 189
- Dupuis, J., Vennes, S., Bowyer, S., Pradhan, A. K., & Thejll, P. 1995, ApJ, 455, 574
- Finley, D. S., Basri, G., & Bowyer, S. 1990, ApJ, 359, 483
- Finley, D. S., Koester, D., & Basri, G. 1997, ApJ, 488, 375
- Fitzpatrick, E. L. 1999, PASP, 111, 63
- Giannicchele, N., Bergeron, P., & Dufour, P. 2012, ApJS, 199, 29
- Gianninas, A., Bergeron, P., & Ruiz, M. T. 2011, ApJ, 743, 138
- Green, J., Jelinsky, P., & Bowyer, S. 1990, ApJ, 359, 499
- Groenewegen, M. A. T. & Lamers, H. J. G. L. M. 1989, A&AS, 79, 359
- Gunderson, K., Wilkinson, E., Green, J. C., & Barstow, M. A. 2001, ApJ, 562, 992
- Guseinov, O. K., Novruzova, K. I., & Rustamov, I. S. 1983, Ap&SS, 96, 1
- Heber, U., Hamann, W.-R., Hunger, K., et al. 1984a, A&A, 136, 331
- Heber, U., Hunger, K., Jonas, G., & Kudritzki, R. P. 1984b, A&A, 130, 119
- Heber, U., Moehler, S., Napiwotzki, R., Thejll, P., & Green, E. M. 2002, A&A, 383, 938
- Høg, E., Fabricius, C., Makarov, V. V., et al. 2000, A&A, 355, L27
- Holberg, J. B., Ali, B., Carone, T. E., & Polidan, R. S. 1991, ApJ, 375, 716
- Holberg, J. B., Barstow, M. A., Hubeny, I., et al. 2003, in Astronomical Society of the Pacific Conference Series, Vol. 291, Hubble's Science Legacy: Future Optical/Ultraviolet Astronomy from Space, ed. K. R. Sembach, J. C. Blades, G. D. Illingworth, & R. C. Kennicutt, Jr., 383
- Holberg, J. B., Barstow, M. A., & Sion, E. M. 1998, ApJS, 119, 207
- Holberg, J. B., Hubeny, I., Barstow, M. A., et al. 1994, ApJ, 425, L105
- Holberg, J. B., Kidder, K., Liebert, J., & Wesemael, F. 1989, in Lecture Notes in Physics, Berlin Springer Verlag, Vol. 328, IAU Colloq. 114: White Dwarfs, ed. G. Wegner, 188–193
- Holberg, J. B., Sion, E. M., Oswalt, T., et al. 2008, AJ, 135, 1225
- Holberg, J. B., Wesemael, F., & Basile, J. 1986, ApJ, 306, 629
- Hubeny, I., Hummer, D. G., & Lanz, T. 1994, A&A, 282, 151
- Hubeny, I. & Lanz, T. 1995, ApJ, 439, 875
- Hummer, D. G. & Mihalas, D. 1988, ApJ, 331, 794
- Kilkenny, D., Heber, U., & Drilling, J. S. 1988, South African Astronomical Observatory Circular, 12, 1
- Kimble, R. A., Davidsen, A. F., Blair, W. P., et al. 1993, ApJ, 404, 663
- Koester, D. 1991, in IAU Symposium, Vol. 145, Evolution of Stars: the Photospheric Abundance Connection, ed. G. Michaud & A. V. Tutukov, 435
- Koester, D. & Finley, D. 1992, in Lecture Notes in Physics, Berlin Springer Verlag, Vol. 401, The Atmospheres of Early-Type Stars, ed. U. Heber & C. S. Jeffery, 314
- Koester, D., Schulz, H., & Weidemann, V. 1979, A&A, 76, 262
- Kurucz, R. L. 1991, in NATO ASIC Proc. 341: Stellar Atmospheres - Beyond Classical Models, ed. L. Crivellari, I. Hubeny, & D. G. Hummer, 441
- Kurucz, R. L. 2009, in American Institute of Physics Conference Series, Vol. 1171, American Institute of Physics Conference Series, ed. I. Hubeny, J. M. Stone, K. MacGregor, & K. Werner, 43
- Kurucz, R. L. 2011, Canadian Journal of Physics, 89, 417
- Kwok, S., Purton, C. R., & Fitzgerald, P. M. 1978, ApJ, 219, L125
- Lajoie, C.-P. & Bergeron, P. 2007, ApJ, 667, 1126
- Landolt, A. U. & Uomoto, A. K. 2007, AJ, 133, 768
- Lanz, T., Barstow, M. A., Hubeny, I., & Holberg, J. B. 1996, ApJ, 473, 1089
- Latour, M., Fontaine, G., Chayer, P., & Brassard, P. 2013, ArXiv e-prints
- Lemoine, M., Vidal-Madjar, A., Hébrard, G., et al. 2002, ApJS, 140, 67
- Liebert, J., Bergeron, P., & Holberg, J. B. 2005, ApJS, 156, 47
- McCook, G. P. & Sion, E. M. 1999, ApJS, 121, 1
- Morton, D. C. 2000, ApJS, 130, 403
- Napiwotzki, R. & Rauch, T. 1994, A&A, 285, 603
- Oegerle, W. R., Jenkins, E. B., Shelton, R. L., Bowen, D. V., & Chayer, P. 2005, ApJ, 622, 377
- Pancino, E., Altavilla, G., Marinoni, S., et al. 2012, MNRAS, 426, 1767
- Preval, S. P., Barstow, M. A., Holberg, J. B., & Dickinson, N. J. 2013, in Astronomical Society of the Pacific Conference Series, Vol. 469, Astronomical Society of the Pacific Conference Series, ed. J. Krzesiński, G. Stachowski, P. Moskalik, & K. Bajan, 193
- Rauch, T. 1997, A&A, 320, 237
- Rauch, T. 2003, A&A, 403, 709
- Rauch, T. 2008a, in Astronomical Spectroscopy and Virtual Observatory, ed. M. Guainazzi & P. Osuna (European Space Agency), 183
- Rauch, T. 2008b, A&A, 481, 807
- Rauch, T. 2012, ArXiv 1210.7636
- Rauch, T. & Deetjen, J. L. 2003, in Astronomical Society of the Pacific Conference Series, Vol. 288, Stellar Atmosphere Modeling, ed. I. Hubeny, D. Mihalas, & K. Werner, 103
- Rauch, T. & Nickelt, I. 2009, in Multi-wavelength Astronomy and Virtual Observatory, ed. D. Baines & P. Osuna, 49
- Rauch, T., Nickelt, I., Stampa, U., Demleitner, M., & Koesterke, L. 2009, in Astronomical Society of the Pacific Conference Series, Vol. 411, Astronomical Data Analysis Software and Systems XVIII, ed. D. A. Bohlender, D. Durand, & P. Dowler, 388
- Rauch, T. & Ringat, E. 2011, in Astronomical Society of the Pacific Conference Series, Vol. 442, Astronomical Data Analysis Software and Systems XX, ed. I. N. Evans, A. Accomazzi, D. J. Mink, & A. H. Rots, 563
- Rauch, T., Ringat, E., & Werner, K. 2010, ArXiv 1011.3628
- Rauch, T., Werner, K., Biémont, É., Quinet, P., & Kruk, J. W. 2012, A&A, 546, A55
- Rauch, T., Ziegler, M., Werner, K., et al. 2007, A&A, 470, 317
- Renedo, I., Althaus, L. G., Miller Bertolami, M. M., et al. 2010, ApJ, 717, 183
- Ringat, E. & Rauch, T. 2010, in American Institute of Physics Conference Series, Vol. 1273, American Institute of Physics Conference Series, ed. K. Werner & T. Rauch, 121–124
- Ringat, E., Rauch, T., & Werner, K. 2012, Baltic Astronomy, 21, 341
- Sahu, M. S., Landsman, W., Bruhwiler, F. C., et al. 1999, ApJ, 523, L159
- Savitzky, A. & Golay, M. J. E. 1964, Analytical Chemistry, 36, 1627
- Schuh, S. L., Dreizler, S., & Wolff, B. 2002, A&A, 382, 164
- Seaton, M. J., Yan, Y., Mihalas, D., & Pradhan, A. K. 1994, MNRAS, 266, 805
- Shipman, H. L. 1979, ApJ, 228, 240
- Tremblay, P.-E. & Bergeron, P. 2009, ApJ, 696, 1755
- van Leeuwen, F. 2007, A&A, 474, 653
- Vennes, S., Chayer, P., & Dupuis, J. 2005, ApJ, 622, L121
- Vennes, S., Chayer, P., Hurwitz, M., & Bowyer, S. 1996, ApJ, 468, 898
- Vennes, S. & Lanz, T. 2001, ApJ, 553, 399
- Vennes, S., Polomski, E. F., Lanz, T., et al. 2000, ApJ, 544, 423
- Vennes, S., Thejll, P., & Shipman, H. L. 1991, in NATO ASIC Proc. 336: White Dwarfs, ed. G. Vauclair & E. Sion, 235
- Vernet, J., Dekker, H., D'Odorico, S., et al. 2011, A&A, 536, A105
- Vernet, J., Kerber, F., D'Odorico, S., et al. 2008a, in 2007 ESO Instrument Calibration Workshop, ed. A. Kaufer & F. Kerber, 153
- Vernet, J., Kerber, F., Mainieri, V., et al. 2010, Highlights of Astronomy, 15, 535
- Vernet, J., Kerber, F., Saitta, F., et al. 2008b, in Society of Photo-Optical Instrumentation Engineers (SPIE) Conference Series, Vol. 7016, Society of Photo-Optical Instrumentation Engineers (SPIE) Conference Series
- Vidal-Madjar, A., Allard, N. F., Koester, D., et al. 1994, A&A, 287, 175
- Vidal-Madjar, A., Lemoine, M., Ferlet, R., et al. 1998, A&A, 338, 694
- Wassermann, D., Werner, K., Rauch, T., & Kruk, J. W. 2010, A&A, 524, A9
- Werner, K., Deetjen, J. L., Dreizler, S., et al. 2003, in Astronomical Society of the Pacific Conference Series, Vol. 288, Stellar Atmosphere Modeling, ed. I. Hubeny, D. Mihalas, & K. Werner, 31
- Werner, K. & Dreizler, S. 1994, A&A, 286, L31
- Werner, K., Rauch, T., Ringat, E., & Kruk, J. W. 2012, ApJ, 753, L7
- Wolff, B., Koester, D., Dreizler, S., & Haas, S. 1998, A&A, 329, 1045
- Ziegler, M., Rauch, T., Werner, K., Köppen, J., & Kruk, J. W. 2012, A&A, 548, A109

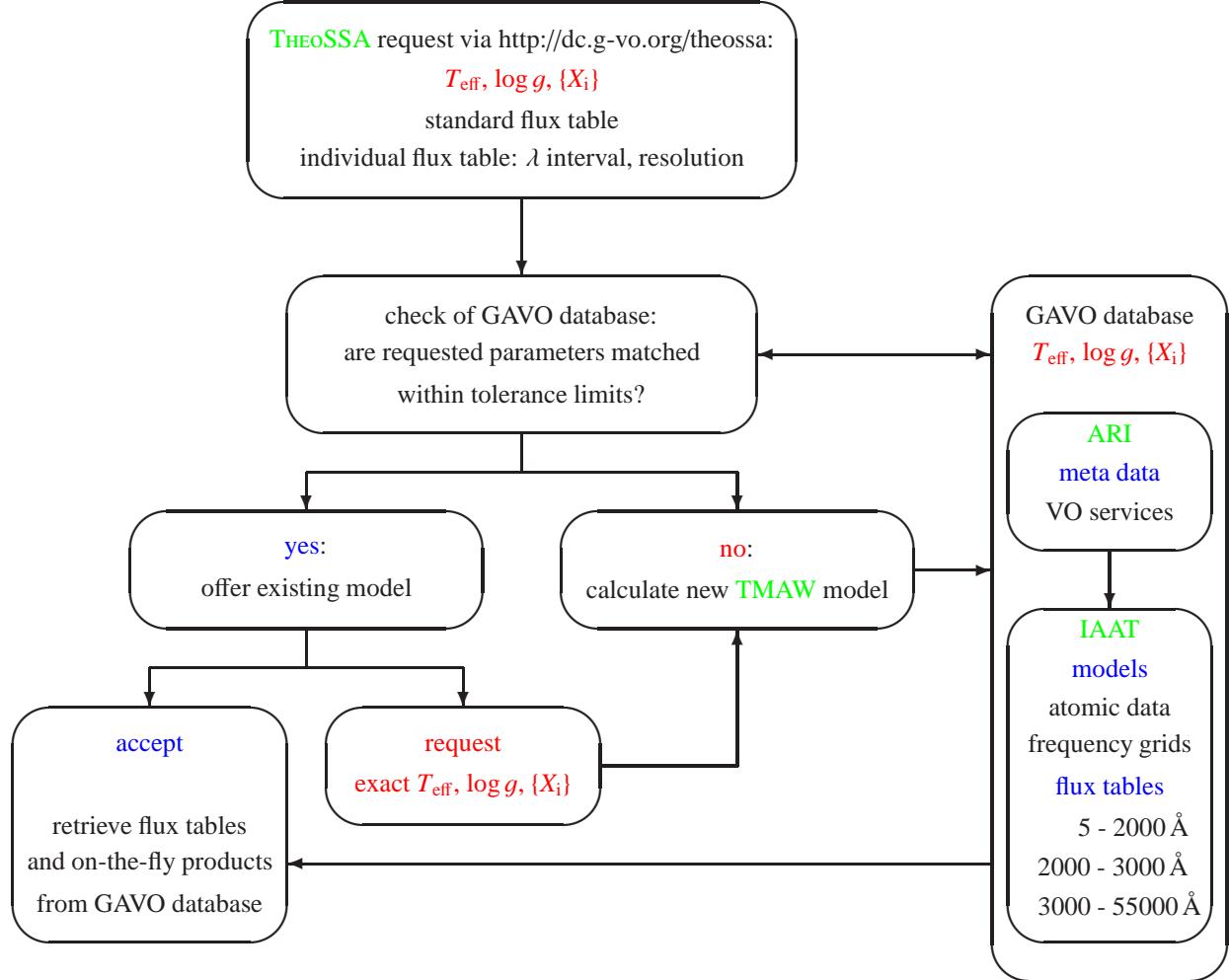


Fig. 1. Flow diagram of TheoSSA. The VO user sends an SED request to the GAVO database by entering the photospheric parameters. If a suitable model is available within the desired tolerance limits, it is offered as a results table. In case that the parameters are not exactly matched, the VO user may decide to calculate a model with the exact parameters. TMAW will start a model-atmosphere calculation at our institute's (IAAT) PC cluster then. Extended model grids make use of compute resources that are provided by AstroGrid-D. As soon as the model is converged, the VO user can retrieve the SED table from the GAVO database.

Table 4. Statistics of our model atoms. IG denotes a generic model atom consisting of Ca, Sc, Ti, V, Cr, Mn, and Co. “sample lines” are individual Kurucz’ lines that are sampled to superlines for Ca - Ni (Rauch & Deetjen 2003).

ion	NLTE levels	LTE levels	lines	sample lines
H I	14	2	91	
II	1	—	—	
He I	29	74	69	
II	16	16	120	
III	1	—	—	
C II	1	45	0	
III	44	23	190	
IV	54	4	295	
V	1	0	0	
N II	1	246	0	
III	34	32	129	
IV	90	4	546	
V	54	8	297	
VI	1	0	0	
O II	1	46	0	
III	72	0	322	
IV	38	56	173	
V	76	50	472	
VI	54	8	291	
VII	1	0	0	
Al II	1	4	0	
III	7	29	10	
IV	6	183	3	
V	6	223	4	
VI	1	0	0	
Si III	17	17	28	
IV	16	7	44	
V	1	0	0	
P III	3	7	0	
IV	21	30	9	
V	18	7	12	
VI	1	0	0	
S III	1	230	0	
IV	17	83	32	
V	39	71	107	
VI	25	12	48	
VII	1	0	0	
Fe III	7	0	25	537 689
IV	7	0	25	3 102 371
V	7	0	25	3 266 247
VI	7	0	33	991 935
VII	7	0	39	200 455
VIII	1	0	0	0
Ni III	7	0	22	1 033 920
IV	7	0	25	2 512 561
V	7	0	27	2 766 664
VI	7	0	27	7 408 657
VII	7	0	33	4 195 381
VIII	1	0	0	0
IG III	1	0	0	0
IV	7	0	25	1 579 918
V	7	0	23	2 230 921
VI	7	0	25	1 455 521
VII	7	0	24	1 129 512
VIII	1	0	0	0

Table 4. continued.

ion	NLTE levels	LTE levels	lines	sample lines
Zn II	1	5	0	
III	2	10	0	
IV	31	0	87	
V	5	15	0	
VI	1	0	0	
Ge III	1	15	0	
IV	8	1	8	
V	85	0	878	
VI	11	25	0	
VII	1	0	0	
Sn III	3	18	2	
IV	6	4	1	
V	5	4	0	
VI	6	0	0	
VII	1	0		
total	70	1038	1614	4646 32 411 752

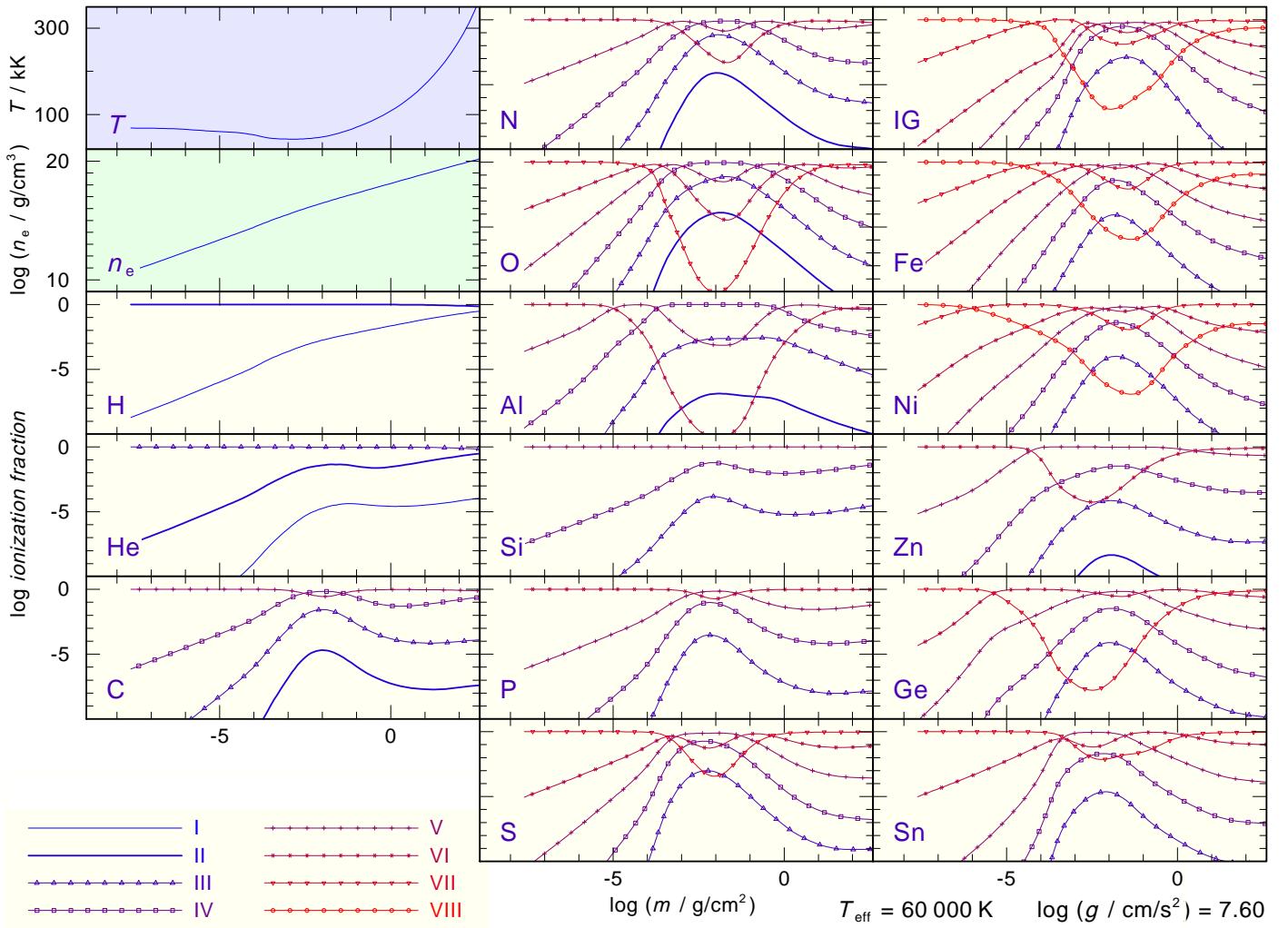


Fig. 6. Temperature and density structure and ionizations fractions of our model with $T_{\text{eff}} = 60\,000$ K and $\log g = 7.60$. IG denotes a generic model atom consisting of Ca, Sc, Ti, V, Cr, Mn, and Co.

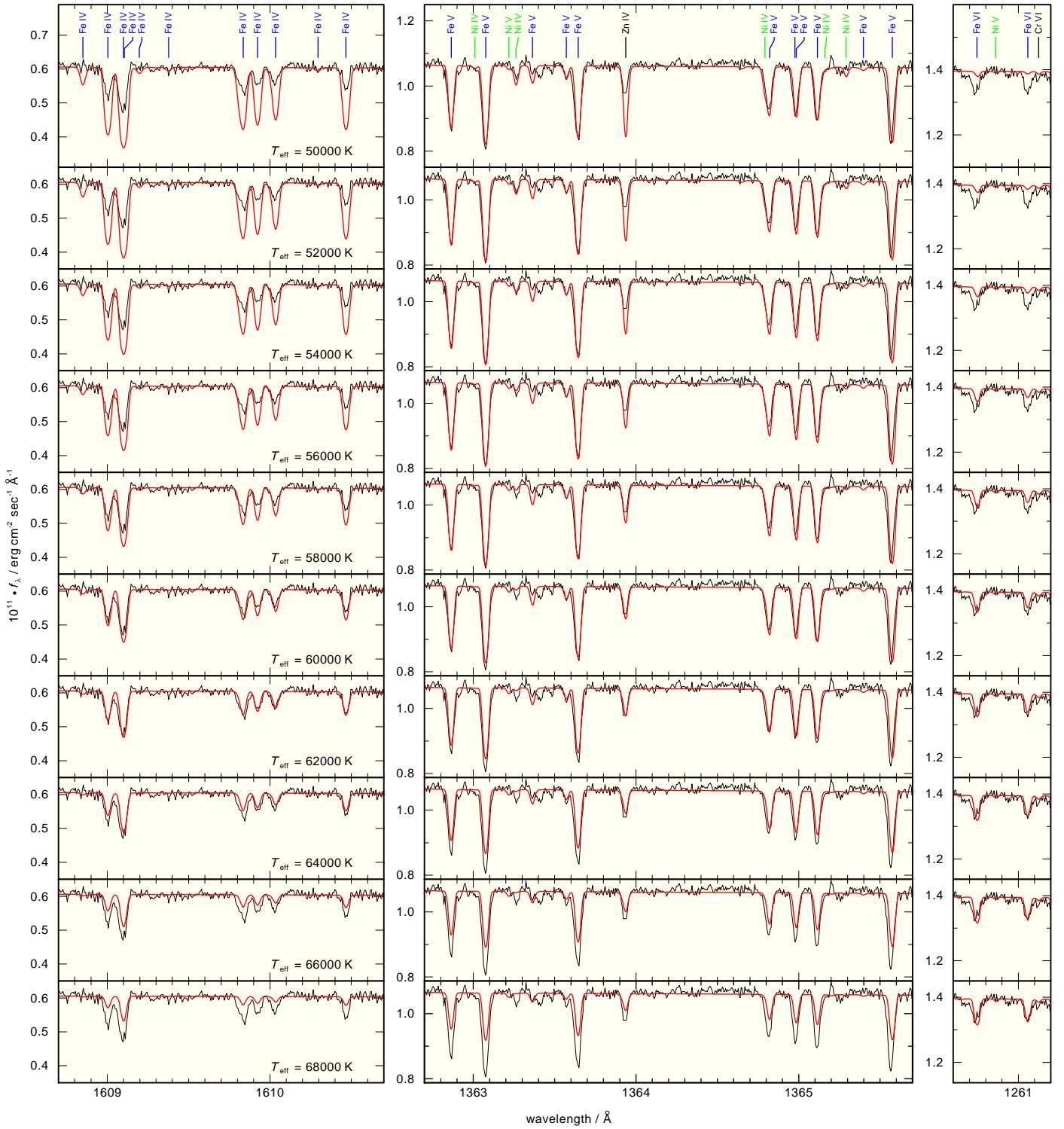


Fig. 11. Same as Fig. 10 for Fe iv - vi lines (from left to right panels, marked blue in the top panels) only.

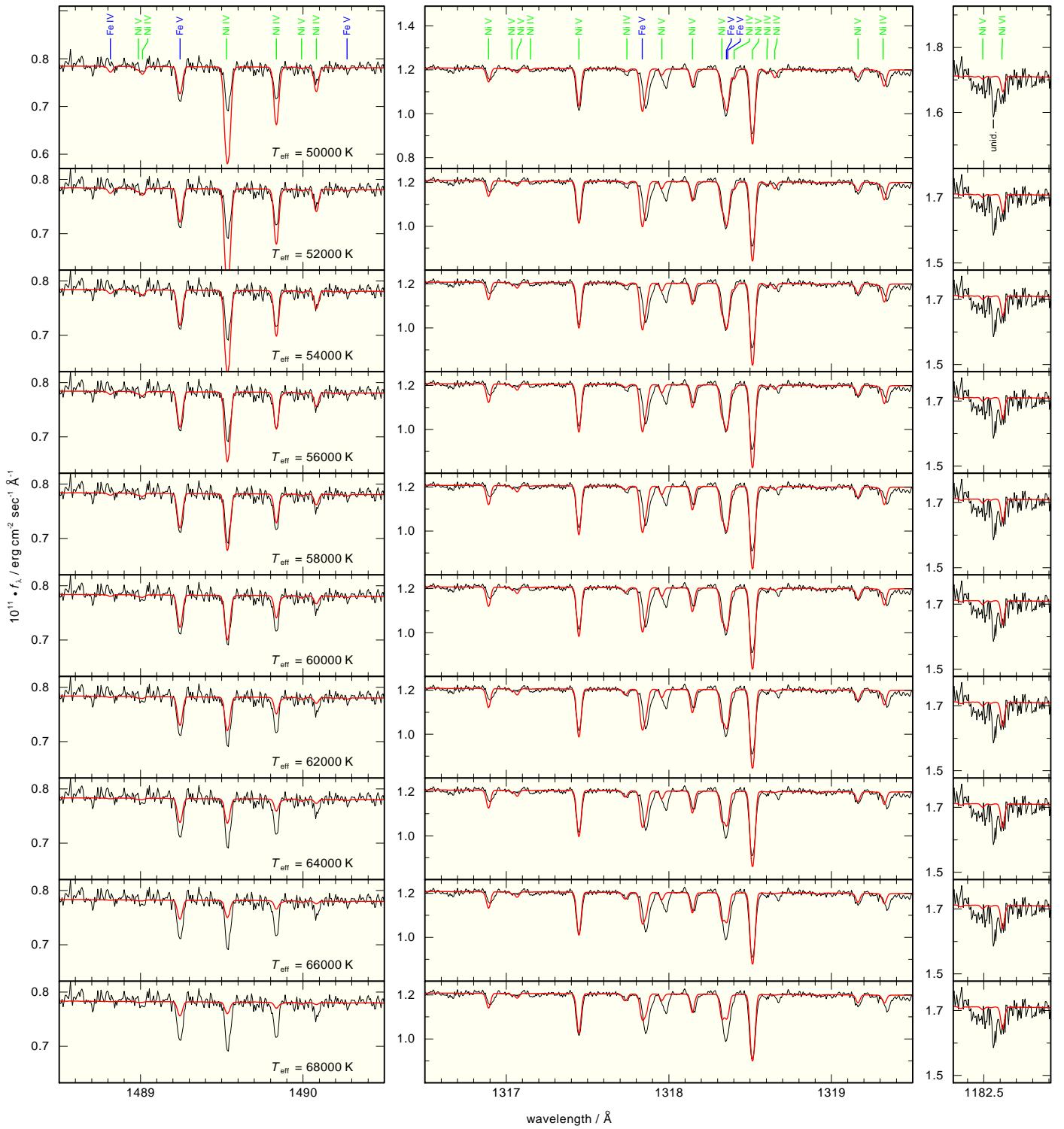


Fig. 12. Same as Fig. 10 for Ni iv - vi lines (from left to right panels, marked green in the top panels) only.

Table 5. Identified lines. λ_{rest} is the wavelength in the stellar rest frame as given by Kurucz (iron-group elements) or NIST. λ_{theo} is the theoretical wavelength of lines with ISM origin. The V, Cr, Mn, and Co line identifications are uncertain.

$\lambda_{\text{rest}} / \text{\AA}$	ion	$\lambda_{\text{theo}} / \text{\AA}$	comment	$\lambda_{\text{rest}} / \text{\AA}$	ion	$\lambda_{\text{theo}} / \text{\AA}$	comment
913.173	H I	913.215	ISM	1347.210	Ni v		
913.298	H I	913.339	ISM	1347.720	Ni v		
913.439	H I	913.480	ISM	1347.952	Zn iv		
913.600	H I	913.641	ISM	1348.843	Fe v		
913.784	H I	913.826	ISM	1349.154	Ni iv		
913.997	H I	914.039	ISM	1349.335	Ni v		
914.245	H I	914.286	ISM	1349.783	Ni v		
914.535	H I	914.576	ISM	1349.874	Zn iv		
914.878	H I	914.919	ISM	1350.036	Ni v		
915.288	H I	915.329	ISM	1350.206	Ni iv		
915.563	N II	915.613	ISM	1350.218	Ni iv		
915.783	H I	915.824	ISM	1350.286	Fe v		
916.388	H I	916.429	ISM	1350.521	Ni iv		
917.139	H I	917.181	ISM	1350.525	Ni v		
918.088	H I	918.129	ISM	1350.672	Fe v		
919.310	H I	919.351	ISM	1350.931	Fe v		
920.922	H I	920.963	ISM	1351.412	Ni v		
921.994	N IV			1351.419	Ni iv		
922.519	N IV			1351.757	Fe v		
923.109	H I	923.150	ISM	1352.602	Fe v		
923.220	N IV			1352.881	Zn iv		
923.676	N IV			1353.112	Ni v		
924.220	S V			1353.737	Fe v		
926.184	H I	926.226	ISM	1353.839	Ni v		
929.470	O I	929.517	ISM	1354.846	Fe v		
930.706	H I	930.748	ISM	1355.535	Ni v		
933.378	S VI			1355.627	Fe v		
936.585	O I	936.630	ISM	1356.079	Ni iv		
937.761	H I	937.803	ISM	1356.169	Zn iv		
944.523	S VI			1356.193	Zn iv		
948.640	O I	948.686	ISM	1356.237	Fe v		
948.643	H I	948.686	ISM	1357.064	Ni iv		
950.657	P IV			1357.112	Fe v		
950.863	Cr IV			1357.242	Fe iv		
953.372	N I	953.415	ISM	1357.478	Ni v		
953.612	N I	953.655	ISM	1357.679	Fe v		
953.927	N I	953.970	ISM	1357.799	Zn iv		
955.334	N IV			1357.854	Fe v		
958.508	Ge v			1358.288	Fe vi		
963.013	Zn iv			1358.327	Ni v		
963.750	P II	963.800	ISM	1358.382	Fe v		
963.944	N II	963.990	ISM	1358.565	Fe v		
964.601	N I	964.626	ISM	1358.683	Fe vi		
964.961	Zn iv			1358.967	Fe v		
965.997	Zn iv			1359.006	Fe v		
966.310	Fe v			1359.148	Fe v		
971.705	O I	971.737	ISM	1359.237	Ni iv		
971.705	O I	971.738	ISM	1359.391	Fe iv		
971.706	O I	971.738	ISM	1359.394	Ni iv		
972.253	D I	972.272	ISM	1359.405	Fe v		
972.493	H I	972.537	ISM	1359.503	Ni v		
976.424	O I	976.448	ISM	1360.215	Ni iv		
977.007	C III	977.020	ISM	1361.268	Ni iv		
977.020	C III			1361.278	Fe v		
978.837	Fe v			1361.446	Fe v		
979.563	Fe v			1361.659	Fe v		
979.768	N III			1361.691	Fe v		
979.832	N III			1361.826	Fe v		

Table 5. continued.

$\lambda_{\text{rest}} / \text{\AA}$	ion	$\lambda_{\text{theo}} / \text{\AA}$	comment	$\lambda_{\text{rest}} / \text{\AA}$	ion	$\lambda_{\text{theo}} / \text{\AA}$	comment
979.905	N III			1362.704	Ni v		
979.969	N III			1362.864	Fe v		
980.623	Zn IV			1363.076	Fe v		
980.813	Fe v			1363.219	Ni v		
981.254	O III			1363.221	Ni v		
981.314	Fe v			1363.222	Ni v		
981.885	Fe v			1363.263	Ni iv		
982.639	Fe v			1363.349	Ni v		
982.856	Fe v			1363.364	Fe v		
982.912	Fe v			1363.455	Fe v		
982.928	Fe v			1363.572	Fe v		
983.009	Fe v			1363.644	Fe v		
983.282	Fe v			1363.910	Zn IV		
983.696	O IV			1364.793	Ni iv		
983.972	Fe v			1364.985	Fe v		
984.178	Fe v			1365.162	Ni iv		
984.407	Fe v			1365.575	Fe v		
984.921	Ge v			1365.868	Fe v		
985.673	Fe v			1365.872	Ni v		
986.266	O IV			1366.005	Ni v		
986.766	Ge v			1366.122	Fe v		
987.683	Fe II	987.687	ISM	1367.174	Fe v		
988.130	Ge v			1368.369	Ni v		
988.459	Fe v			1369.508	Zn IV		
988.571	O I	988.578	ISM	1370.302	Fe v		
988.648	O I	988.655	ISM	1370.734	Fe vi		
988.767	O I	988.773	ISM	1370.753	Mn iv		
989.745	S I	989.870	ISM	1370.943	Fe v		
989.799	N III			1371.073	Fe vi		
989.799	O v			1371.123	Fe v		
989.842	S I	989.870	ISM	1371.204	Ni v		
989.878	O v			1371.215	Fe v		
990.289	Fe v			1371.296	O v		
990.666	Ge v			1371.411	Ni iv		
990.846	Fe v			1371.555	Fe iv		
991.002	Fe v			1371.680	Ni iv		
991.131	Fe v			1371.778	Ni iv		
991.264	Fe v			1371.983	Fe v		
991.511	N III			1372.653	Fe v		
991.577	N III			1373.392	Ni v		
991.955	Fe v			1373.589	Fe v		
992.305	Ge v			1373.679	Fe v		
992.522	Fe v			1373.964	Fe v		
992.716	Fe v			1374.119	Fe v		
992.857	Fe v			1374.253	Fe v		
993.051	Fe v			1374.629	Fe vi		
993.280	Fe v			1374.788	Fe v		
993.753	Fe v			1374.805	Fe v		
993.838	Fe v			1375.323	Zn IV		
994.142	Fe v			1375.374	Ni v		
994.234	Fe v			1375.506	Cr iv		
994.260	Fe v			1375.790	Fe v		
994.399	Fe v			1376.337	Fe v		
994.834	Fe v			1376.451	Fe v		
994.931	Fe v			1377.613	Zn IV		
995.256	Fe v			1377.707	Ni v		
995.322	Fe iv			1378.088	Fe v		
995.661	Fe v			1378.561	Fe v		
995.738	Fe v			1378.708	Ni iv		
996.576	Fe v			1379.040	Fe v		

Table 5. continued.

$\lambda_{\text{rest}} / \text{\AA}$	ion	$\lambda_{\text{theo}} / \text{\AA}$	comment	$\lambda_{\text{rest}} / \text{\AA}$	ion	$\lambda_{\text{theo}} / \text{\AA}$	comment
996.753	Fe v			1379.202	Fe v		
996.965	Fe v			1380.112	Fe v		
997.115	Fe v			1381.309	Ni iv		
997.412	Fe v			1381.517	Fe iv		
997.466	Fe v			1382.266	Fe v		
997.543	P v			1382.420	Fe v		
997.613	P v			1382.506	Ni v		
997.823	Fe v			1383.811	Ni iv		
997.904	Fe v			1384.058	Fe v		
998.014	Fe v			1384.130	Al iii		
998.093	Fe v			1384.200	Fe v		
998.116	Fe v			1384.685	Fe v		
998.285	Fe v			1384.854	Ni v		
998.691	Fe v			1385.684	Fe v		
999.619	Fe v			1385.761	Ni iv		
999.763	Fe v			1385.865	Ni v		
1000.140	Fe v			1386.176	Ni iv		
1000.391	Ni vi			1386.234	Ni v		
1000.766	Fe v			1386.270	Ni iv		
1000.931	Fe vi			1386.270	Ni iv		
1001.191	Fe v			1386.468	Fe v		
1001.451	Fe v			1386.730	Ni iv		
1001.557	Fe v			1387.095	Fe v		
1001.666	Fe v			1387.163	Ni v		
1001.944	Zn iv			1387.692	Zn iv		
1002.112	Fe v			1387.937	Fe v		
1002.304	Fe v			1388.044	Fe v		
1002.550	Fe v			1388.195	Fe v		
1002.675	Fe v			1388.324	Fe v		
1002.803	Fe v			1388.548	Fe v		
1002.871	Fe v			1388.993	Ni v		
1003.088	Fe iv			1389.005	Fe v		
1003.225	Ge v			1389.063	Ni v		
1003.680	Fe v			1389.435	Ni v		
1003.933	Fe v			1390.910	Ni v		
1004.082	Ge v			1390.971	Fe v		
1004.589	Fe v			1391.204	Zn iv		
1004.910	Fe v			1392.277	Fe v		
1004.937	Ge v			1392.476	Ni v		
1005.003	Fe v			1393.072	Fe v		
1005.167	Fe v			1393.755	Si iv		
1005.959	Fe v			1394.270	Fe v		
1006.051	Fe v			1394.370	Ni v		
1006.232	Fe v			1394.671	Fe v		
1006.590	Fe v			1394.799	Fe v		
1006.727	Fe v			1394.835	Fe iv		
1006.852	Fe v			1395.442	Fe v		
1007.120	Fe v			1395.979	Ni iv		
1007.292	Fe v			1396.081	Fe v		
1007.450	Fe v			1396.145	Fe v		
1008.151	Fe v			1396.252	Fe iv		
1008.380	Fe v			1396.533	Ni iv		
1009.277	Fe v			1396.584	Ni iv		
1009.375	Fe v			1397.110	Fe v		
1009.596	Fe v			1397.319	Ni v		
1009.802	Fe v			1397.374	Ni iv		
1009.976	Fe v			1397.546	Ni v		
1010.140	Fe v			1397.751	Fe v		
1010.252	Fe v			1397.974	Fe v		
1010.352	Fe v			1398.020	Fe iv		

Table 5. continued.

$\lambda_{\text{rest}} / \text{\AA}$	ion	$\lambda_{\text{theo}} / \text{\AA}$	comment	$\lambda_{\text{rest}} / \text{\AA}$	ion	$\lambda_{\text{theo}} / \text{\AA}$	comment
1010.691	Fe v			1398.161	Fe v		
1011.367	Fe v			1398.193	Ni iv		
1011.512	Fe v			1398.873	Ni iv		
1011.596	Zn iv			1399.947	Ni iv		
1012.124	Fe v			1400.237	Fe v		
1012.178	Zn iv			1400.348	Ni iv		
1012.236	Fe v			1400.376	Ni iv		
1012.370	Fe v			1400.501	Fe v		
1012.814	Fe v			1400.682	Ni iv		
1013.831	Fe v			1400.784	Ni iv		
1014.007	Fe v			1401.267	Ni v		
1015.333	Fe v			1401.897	Ni iv		
1015.508	Fe v			1402.385	Fe v		
1015.701	Ge v			1402.389	Ni iv		
1016.667	Ge v			1402.391	Fe v		
1016.824	Fe v			1402.542	Ni iv		
1016.998	Fe v			1402.770	Si iv		
1017.387	Fe v			1403.369	Fe v		
1017.901	O v			1405.359	Fe v		
1018.124	Ge v			1405.966	Fe v		
1018.265	Ge v			1406.454	Ni iv		
1025.419	D I	1025.440	ISM	1406.668	Fe v		
1025.562	P IV			1406.824	Fe v		
1025.676	H I	1025.722	ISM	1406.864	Fe v		
1028.094	P IV			1407.010	Fe v		
1030.514	P IV			1407.248	Fe v		
1030.515	P IV			1407.440	Ni iv		
1030.548	Ni vi			1407.778	Fe iv		
1031.912	O vi			1408.118	Fe v		
1033.105	Ge v			1408.715	Ni iv		
1033.112	P IV			1408.800	Fe v		
1035.503	Ge v			1409.026	Fe v		
1035.516	Ni vi			1409.225	Fe v		
1035.516	P IV			1409.384	Zn iv		
1035.857	Fe v			1409.453	Fe v		
1036.292	C II	1036.337	ISM	1409.479	Fe v		
1036.531	Zn iv			1409.708	Ni vi		
1036.579	Zn iv			1409.845	Ni iv		
1036.973	C II	1037.018	ISM	1409.851	Fe v		
1037.613	O vi			1410.020	Ni iv		
1038.007	Ge v			1410.161	Fe v		
1038.622	O I	1038.657	ISM	1411.070	Fe v		
1038.657	Fe v			1411.229	Ni iv		
1039.081	Fe v			1411.451	Ni iv		
1039.195	O I	1039.230	ISM	1411.566	Fe v		
1039.684	Zn iv			1411.939	Ni iv		
1039.916	S v			1414.251	Fe iv		
1042.201	Fe v			1414.597	Ni iv		
1043.614	Fe v			1414.777	Ni iv		
1043.991	Fe v			1414.831	Fe v		
1044.474	Zn iv			1415.140	Fe v		
1045.712	Ge v			1415.200	Fe v		
1046.186	Fe v			1415.540	Fe v		
1046.321	Fe v			1416.222	Fe v		
1048.201	Ar I	1048.220	ISM	1416.419	Ni iv		
1049.674	Fe v			1416.531	Ni iv		
1050.056	Ge v			1416.958	Ni iv		
1053.957	Fe v			1417.003	Fe v		
1054.588	Ge v			1417.237	Si iii		
1056.985	Fe v			1417.278	Ni iv		

Table 5. continued.

$\lambda_{\text{rest}} / \text{\AA}$	ion	$\lambda_{\text{theo}} / \text{\AA}$	comment	$\lambda_{\text{rest}} / \text{\AA}$	ion	$\lambda_{\text{theo}} / \text{\AA}$	comment
1058.662	Zn iv			1418.124	Fe v		
1062.664	S iv			1418.343	Ni iv		
1062.986	Fe v			1419.126	Ni iv		
1064.143	Fe v			1419.295	Fe v		
1064.287	Fe v			1419.450	Ni iv		
1066.614	Si iv			1419.577	Ni iv		
1066.636	Si iv			1419.741	Fe v		
1066.650	Si iv			1420.126	Ni iv		
1067.557	Ge v			1420.214	Ni iv		
1068.088	Ge v			1420.352	Fe v		
1069.484	Fe v			1420.424	Fe v		
1071.896	Fe v			1420.477	Fe v		
1072.191	Fe v			1420.606	Fe v		
1072.659	Ge v			1420.749	Fe v		
1072.974	S iv			1421.014	Fe v		
1073.518	S iv			1421.216	Ni iv		
1074.338	Fe v			1421.992	Fe iv		
1074.409	Fe v			1422.132	Fe iv		
1083.932	N ii	1083.990	ISM	1422.479	Fe v		
1086.651	Ge v			1422.607	Ni iv		
1087.854	Ge v			1422.928	Fe iv		
1089.489	Ge v			1423.146	Fe iv		
1092.088	Ge v			1423.439	Ni iv		
1096.773	Fe v			1423.478	Fe iv		
1098.929	S iv			1423.536	Ni iv		
1099.480	S iv			1425.086	Fe v		
1101.921	Fe v			1425.479	Fe iv		
1106.715	Fe v			1425.729	Fe iv		
1107.591	C iv			1426.047	Fe iv		
1107.930	C iv			1426.238	Fe iv		
1107.979	C iv			1426.371	Ni iv		
1109.889	Zn iv			1427.271	Fe iv		
1109.940	Si iii			1427.346	Fe iv		
1109.970	Si iii			1427.452	Ni iv		
1111.829	Fe v			1427.507	Fe iv		
1112.648	Fe v			1427.554	Fe iv		
1113.174	Si iii			1427.815	Fe v		
1113.204	Si iii			1428.933	Ni iv		
1113.230	Si iii			1429.006	Fe v		
1114.052	Fe v			1429.312	Fe iv		
1115.070	Fe v			1429.470	Fe v		
1116.050	Fe v			1429.492	Fe v		
1116.162	Fe v			1430.190	Ni iv		
1116.807	Fe v			1430.312	Fe v		
1116.947	Ge v			1430.520	Fe iv		
1117.977	P v			1430.572	Fe v		
1118.412	C iv			1430.754	Fe v		
1118.552	P iv			1431.012	Ni iv		
1119.200	Fe v			1431.432	Fe iv		
1120.883	Ni v			1431.871	Ni v		
1122.031	S v			1431.941	Ni v		
1122.485	Si iv			1432.449	Ni iv		
1123.744	Ge v			1432.938	Fe v		
1123.752	Ge v			1433.108	Ni iv		
1123.871	Fe v			1433.260	Ni iv		
1124.189	Ni vi			1434.387	Fe iv		
1124.297	Ni v			1435.017	Ni iv		
1125.422	Ge v			1435.048	Fe v		
1127.056	S v			1435.243	Ni iv		
1127.196	Ni vi			1437.164	Ni iv		

Table 5. continued.

$\lambda_{\text{rest}} / \text{\AA}$	ion	$\lambda_{\text{theo}} / \text{\AA}$	comment	$\lambda_{\text{rest}} / \text{\AA}$	ion	$\lambda_{\text{theo}} / \text{\AA}$	comment
1128.008	P v			1437.387	Ni iv		
1128.325	Si iv			1437.525	Sn iv		
1128.340	Si iv			1437.937	Ni iv		
1128.666	S v			1438.112	Fe v		
1128.779	S v			1438.791	Fe v		
1129.207	Fe v			1438.814	Ni iv		
1130.043	Ni v			1439.039	Ni iv		
1130.485	Ni vi			1439.050	Fe v		
1130.507	Fe v			1439.052	Ni iv		
1130.590	Fe v			1439.584	Ni iv		
1130.952	Fe v			1439.685	Fe iv		
1131.604	Ni vi			1439.775	Ni iv		
1133.567	Co vi			1439.993	Ni v		
1133.908	Ni iv			1440.528	Fe v		
1134.110	N ii	1134.165	ISM	1440.615	Ni iv		
1134.360	N ii	1134.415	ISM	1440.793	Fe v		
1134.925	N ii	1134.980	ISM	1440.945	Fe iv		
1143.175	Fe ii	1143.226	ISM	1441.049	Fe v		
1144.035	Ni vi			1441.182	Ni iv		
1144.290	Ni vi			1441.620	Ni iv		
1144.938	Fe ii	1144.938	ISM	1441.691	Ni iv		
1149.116	Fe v			1442.130	Ni iv		
1150.089	Ni v			1442.215	Fe v		
1150.501	Zn iv			1442.414	Ni iv		
1151.059	Ni v			1442.500	Ni iv		
1151.263	Ni vi			1442.702	Ni iv		
1151.665	Fe v			1442.802	Fe v		
1151.960	Ni v			1443.087	Fe v		
1152.406	Ni v			1443.168	Fe v		
1152.675	Ni v			1444.143	Ni iv		
1152.792	Ni v			1444.288	Fe iv		
1153.109	Ni vi			1444.394	Fe v		
1153.647	Ni vi			1444.395	Fe iv		
1153.778	Fe v			1444.431	Ni iv		
1154.433	Zn iv			1444.913	Ni iv		
1154.605	Ni vi			1445.078	Ni iv		
1155.824	Zn iv			1445.078	Ni iv		
1157.551	Ni vi			1445.686	Fe v		
1158.115	Ni v			1445.912	Fe v		
1158.998	Ni vi			1446.002	Fe iv		
1159.023	Ni v			1446.157	Fe iv		
1159.177	Ni vi			1446.286	Fe v		
1160.509	Fe vi			1446.579	Fe v		
1161.894	Fe v			1446.617	Fe v		
1161.950	Ni vi			1447.589	Ni iv		
1162.010	Ni vi			1447.704	Fe v		
1163.251	Ni vi			1447.751	Fe iv		
1163.382	Ni vi			1448.488	Fe v		
1163.519	Fe v			1448.847	Fe v		
1163.854	Ni v			1449.021	Ni iv		
1164.151	Fe vi			1449.189	Ni iv		
1164.326	Ni vi			1449.761	Fe v		
1165.671	Fe v			1449.778	Ni iv		
1165.674	Fe vi			1449.887	Fe v		
1167.102	Ni v			1451.101	Fe v		
1167.695	Fe vi			1451.267	Fe v		
1167.751	Ni vi			1451.347	Ni iv		
1167.928	Fe vi			1452.144	Ni iv		
1168.849	C iv			1452.220	Ni iv		
1168.993	C iv			1452.399	Fe iv		

Table 5. continued.

$\lambda_{\text{rest}} / \text{\AA}$	ion	$\lambda_{\text{theo}} / \text{\AA}$	comment	$\lambda_{\text{rest}} / \text{\AA}$	ion	$\lambda_{\text{theo}} / \text{\AA}$	comment
1168.993	C IV			1452.477	Fe IV		
1170.267	Ni V			1452.720	Cr IV		
1170.339	Ni VI			1452.971	Fe V		
1170.845	Ni VI			1453.104	Fe V		
1171.737	Fe V			1453.495	Ni IV		
1171.737	Ni V			1453.617	Fe V		
1173.714	V IV			1454.243	Fe V		
1174.121	Fe IV			1454.364	Ni IV		
1174.195	Ni V			1454.501	Ni IV		
1174.504	Ni IV			1454.580	Fe IV		
1174.590	Ni VI			1454.700	Fe V		
1174.933	C III			1455.272	Ni IV		
1175.263	C III			1455.422	Ni IV		
1175.503	O III			1455.555	Fe V		
1175.590	C III			1455.602	Ni IV		
1175.711	C III			1455.726	Fe IV		
1175.987	C III			1455.897	Ni IV		
1176.370	C III			1456.162	Fe V		
1176.912	Ni VI			1456.289	Fe V		
1176.946	Ni VI			1456.524	Ni IV		
1176.961	Mn VI			1456.750	Fe IV		
1176.966	Ni VI			1457.367	Fe IV		
1176.973	Fe IV			1457.416	Ni IV		
1176.990	Ni V			1457.732	Fe V		
1176.994	Ni V			1457.864	Ni IV		
1177.247	Zn IV			1458.523	Fe IV		
1177.500	Zn IV			1458.764	Fe IV		
1177.867	Fe V			1458.904	Ni IV		
1178.217	Ni VI			1459.253	Fe V		
1178.919	Ni V			1459.769	Fe V		
1179.484	Zn IV			1459.828	Fe V		
1180.245	Ni V			1460.233	Fe IV		
1180.300	Ni VI			1460.547	Ni IV		
1180.388	Ni VI			1460.605	Ni IV		
1180.827	Fe VII			1460.730	Fe V		
1181.576	Zn IV			1460.864	Fe IV		
1182.020	Zn IV			1461.079	Fe IV		
1182.612	Ni VI			1461.433	Ni IV		
1184.253	Ni VI			1461.478	Ni IV		
1184.647	Ni VI			1461.768	Ni IV		
1185.950	Ni V			1462.014	Ni IV		
1189.028	Ge IV			1462.136	Ni IV		
1189.540	Zn IV			1462.239	Fe IV		
1190.143	Si III	1190.203	ISM	1462.636	Fe V		
1190.319	Ni V			1463.672	Ni IV		
1190.363	Si II	1190.416	ISM	1464.221	Fe V		
1190.404	Si II	1190.416	ISM	1464.686	Fe V		
1191.679	Fe V			1464.695	Fe IV		
1192.462	Ni VI			1464.873	Fe V		
1193.240	Si II	1193.290	ISM	1465.006	Fe V		
1193.280	Si II	1193.290	ISM	1465.380	Fe V		
1193.887	Ni VI			1465.401	Fe V		
1194.242	Ni VI			1466.495	Ni IV		
1194.252	Ni V			1466.650	Fe V		
1194.279	Ni V			1466.817	Fe IV		
1194.281	Ni VI			1466.930	Ni IV		
1195.100	Fe V			1466.969	Fe IV		
1195.186	Ni V			1467.134	Ni IV		
1196.101	Ni V			1468.041	Ni IV		
1196.202	Fe V			1468.925	Ni IV		

Table 5. continued.

$\lambda_{\text{rest}} / \text{\AA}$	ion	$\lambda_{\text{theo}} / \text{\AA}$	comment	$\lambda_{\text{rest}} / \text{\AA}$	ion	$\lambda_{\text{theo}} / \text{\AA}$	comment
1196.607	Fe v			1468.998	Fe v		
1197.195	Fe v			1469.598	Fe v		
1197.276	Ni v			1470.422	Ni iv		
1197.385	Ni v			1470.515	Fe iv		
1198.193	Fe vi			1470.731	Fe v		
1198.279	Ni v			1471.207	Fe v		
1198.519	Ni v			1471.333	Fe v		
1199.357	N I	1199.550	ISM	1472.095	Fe v		
1199.403	Ni v			1472.396	Fe iv		
1199.497	N I	1199.550	ISM	1472.511	Fe v		
1199.538	N I	1199.550	ISM	1472.626	Ni iv		
1200.030	N I	1200.223	ISM	1472.804	Fe v		
1200.170	N I	1200.223	ISM	1473.182	Fe iv		
1200.183	Fe v			1474.276	Fe v		
1200.211	N I	1200.223	ISM	1475.311	Ni v		
1200.517	N I	1200.710	ISM	1475.605	Fe v		
1200.657	N I	1200.710	ISM	1476.233	Ni iv		
1200.698	N I	1200.710	ISM	1476.241	Ni iv		
1201.909	Fe v			1476.429	Ni iv		
1202.029	Ni v			1476.579	Ni iv		
1202.432	Ni v			1476.634	Fe v		
1203.270	Ni vi			1476.815	Ni iv		
1203.274	Ni v			1477.485	Ni iv		
1203.274	Ni v			1477.533	Ni vi		
1203.298	Ni iv			1477.581	Ni iv		
1203.300	Ni v			1477.797	Fe v		
1203.301	Ni vi			1477.845	Ni iv		
1203.346	Ni v			1478.044	Ni iv		
1203.765	Ni v			1478.319	Ni iv		
1204.021	Zn iv			1478.364	Fe iv		
1204.075	Fe v			1478.808	Fe iv		
1204.078	Ni vi			1479.209	Ni iv		
1205.303	Ni v			1479.386	Fe v		
1205.447	Ni v			1479.476	Fe v		
1205.601	Ni v			1480.345	Ni iv		
1205.791	Ni v			1481.411	Ni iv		
1205.960	Ni v			1482.248	Ni iv		
1206.041	Fe vi			1482.665	Ni iv		
1206.447	Si iii	1206.500	ISM	1483.113	Fe iv		
1206.500	Si iii			1483.158	Fe iv		
1206.555	Si iii			1483.211	Ni iv		
1207.345	Ni v			1483.259	Fe v		
1207.377	Ni v			1484.212	Fe v		
1207.377	Ni vi			1484.422	Ni iv		
1207.382	Fe iv			1485.017	Fe v		
1207.382	Ni v			1485.114	Ni iv		
1208.196	Ni v			1485.145	Fe v		
1208.259	Fe v			1485.327	Fe iv		
1208.259	Ni v			1485.451	Fe v		
1209.608	Ni v			1486.037	Fe iv		
1209.747	Ni v			1486.195	Ni iv		
1215.132	He ii			1487.004	Ni iv		
1215.321	D I	1215.339	ISM	1487.071	Ni iv		
1215.647	H I	1215.671	ISM	1487.880	Ni iv		
1215.671	H I			1489.243	Fe v		
1221.129	Ni v			1489.529	Ni iv		
1221.875	Ni v			1489.836	Ni iv		
1222.107	Fe v			1490.082	Ni iv		
1222.188	Ni v			1491.020	Zn iv		
1224.546	Ni v			1491.776	Fe v		

Table 5. continued.

$\lambda_{\text{rest}} / \text{\AA}$	ion	$\lambda_{\text{theo}} / \text{\AA}$	comment	$\lambda_{\text{rest}} / \text{\AA}$	ion	$\lambda_{\text{theo}} / \text{\AA}$	comment
1224.759	Ni v			1491.903	Ni iv		
1224.875	Ni v			1492.090	Fe iv		
1224.951	Ni v			1492.646	Ni iv		
1228.436	Ni v			1493.010	Ni iv		
1228.605	Fe vi			1493.023	Fe iv		
1228.681	Fe vi			1493.619	Ni iv		
1228.895	Ni v			1493.672	Ni iv		
1228.962	Fe vi			1495.178	Fe iv		
1229.394	Ni v			1495.618	Fe v		
1229.397	Ni v			1495.797	Ni iv		
1229.839	Ge iv			1496.221	Fe iv		
1229.947	Fe vi			1496.265	Fe v		
1230.047	Ni v			1497.494	Fe iv		
1230.435	Ni v			1497.596	Ni iv		
1230.577	Ni vi			1497.925	Ni iv		
1230.795	Si iv			1498.275	Ni iv		
1230.822	Ni v			1498.698	Ni iv		
1230.890	Ni v			1498.763	Ni iv		
1230.893	Ni v			1498.893	Ni iv		
1231.100	Ni v			1499.113	Ni iv		
1231.875	Ni v			1499.266	Ni iv		
1232.477	Fe vi			1499.442	Fe iv		
1232.524	Ni v			1499.972	Ni iv		
1232.807	Ni v			1500.412	Fe iv		
1232.924	Ni vi			1500.580	Fe v		
1232.964	Ni v			1501.693	Fe iv		
1233.113	Ni v			1501.799	S ,v		
1233.257	Ni v			1501.903	Ni iv		
1233.312	Ni v			1502.651	Fe iv		
1233.508	Ni v			1503.172	Ni iv		
1233.602	Ni v			1503.244	Fe iv		
1233.916	Ni v			1503.479	Ni iv		
1234.096	Ni v			1503.635	Fe v		
1234.163	Ni v			1503.789	Ni iv		
1234.393	Ni v			1504.117	Fe iv		
1234.647	Fe v			1504.329	Fe v		
1234.694	Ni v			1504.389	Fe iv		
1235.831	Ni v			1504.796	Ni iv		
1236.277	Ni v			1505.763	Ni iv		
1236.702	Ni v			1505.765	Fe iv		
1236.973	Fe vi			1505.852	Fe iv		
1237.204	Ni v			1507.061	Ni iv		
1237.336	Ni v			1507.566	Fe iv		
1237.923	Fe v			1508.150	Fe v		
1237.962	Ni v			1509.101	Ni iv		
1237.988	Ni vi			1509.792	Fe v		
1237.995	Ni v			1511.148	Fe iv		
1238.111	Ni v			1511.263	N iv		
1238.217	Ni v			1511.363	Fe iv		
1238.706	Ni v			1511.435	Fe v		
1238.821	N v			1512.050	Fe iv		
1239.552	Ni v			1512.354	Ni iv		
1239.953	Ni v			1512.419	Fe iv		
1240.073	Fe vi			1512.704	Ni iv		
1240.318	Ni v			1512.772	Ni iv		
1240.896	Ni v			1513.102	Ni iv		
1241.015	Ni v			1513.494	Ni iv		
1241.047	Ni v			1513.584	Fe iv		
1241.319	Ni v			1513.979	N iv		
1241.422	Ni v			1514.832	Fe v		

Table 5. continued.

$\lambda_{\text{rest}} / \text{\AA}$	ion	$\lambda_{\text{theo}} / \text{\AA}$	comment	$\lambda_{\text{rest}} / \text{\AA}$	ion	$\lambda_{\text{theo}} / \text{\AA}$	comment
1241.627	Ni v			1514.890	Fe iv		
1241.972	Ni v			1515.434	Zn iv		
1242.071	Ni v			1516.078	Fe iv		
1242.136	Ni v			1516.582	Fe iv		
1242.216	Ni iv			1516.668	Ni iv		
1242.287	Fe v			1516.689	Ni iv		
1242.640	Ni v			1516.799	Fe v		
1242.804	N v			1517.787	Fe v		
1242.976	Ni iv			1519.519	Fe v		
1243.203	Ni v			1519.604	Ni iv		
1243.504	Ni v			1519.930	Fe v		
1243.662	Ni v			1520.418	Fe v		
1244.027	Ni v			1520.510	Ni v		
1244.145	Ni v			1520.621	Ni iv		
1244.174	Ni v			1523.923	Fe iv		
1244.238	Ni v			1524.363	Fe iv		
1244.791	Ni v			1525.031	Fe iv		
1244.958	Ni v			1525.164	Fe v		
1245.020	Ni v			1525.306	Ni iv		
1245.074	Ni v			1525.602	Fe iv		
1245.176	Ni v			1526.066	Fe iv		
1245.203	Ni v			1526.637	Si ii	1526	707.ISM
1245.214	Ni v			1526.691	Si ii	1526	707.ISM
1245.361	Ni v			1526.718	Fe v		
1245.420	Ni v			1526.829	Ni iv		
1245.522	Ni v			1526.906	Fe iv		
1245.620	Ni iv			1527.353	Fe iv		
1246.112	Ni v			1527.685	Ni iv		
1246.358	Ni v			1527.793	Ni iv		
1246.547	Ni v			1528.061	Fe iv		
1246.808	Ni v			1528.484	Fe v		
1246.821	Ni v			1528.935	Fe iv		
1247.383	C iii			1529.943	Ni iv		
1247.479	Ni v			1530.041	Fe iv		
1248.023	Ni v			1530.124	Fe iv		
1248.092	Ni v			1530.256	Fe iv		
1248.156	Fe v			1530.440	Fe v		
1248.232	Ni v			1531.223	Fe iv		
1248.499	Ni v			1531.470	Fe iv		
1248.832	Ni v			1531.738	Ni iv		
1249.522	Ni v			1532.069	Fe iv		
1250.033	Ni v			1532.330	Fe v		
1250.344	Ni v			1532.356	Fe v		
1250.388	Ni v			1532.490	Fe iv		
1250.536	Ni v			1532.630	Fe iv		
1250.736	Fe v			1532.903	Fe iv		
1250.882	Ni v			1533.218	Fe iv		
1251.035	Fe v			1533.267	Fe iv		
1251.812	Ni v			1533.387	Fe v		
1252.075	Ni v			1533.578	Fe iv		
1252.133	Ni v			1533.869	Fe iv		
1252.183	Ni v			1533.949	Fe iv		
1252.267	Ni v			1534.710	Ni iv		
1252.706	Ni v			1534.726	P i	1534	752.ISM
1252.765	Ni v			1535.721	Fe iv		
1252.789	Fe vi			1536.577	Fe iv		
1252.999	Ni v			1536.842	Ni iv		
1253.012	Ni v			1537.248	Ni iv		
1253.191	Ni v			1538.122	Fe iv		
1253.489	Ni v			1538.286	Fe iv		

Table 5. continued.

$\lambda_{\text{rest}} / \text{\AA}$	ion	$\lambda_{\text{theo}} / \text{\AA}$	comment	$\lambda_{\text{rest}} / \text{\AA}$	ion	$\lambda_{\text{theo}} / \text{\AA}$	comment
1253.511	Ni v			1538.923	Ni iv		
1253.637	Ni v			1540.396	Fe iv		
1253.675	Fe vi			1540.729	Fe iv		
1253.755	Si ii	1253.811	ISM	1542.155	Fe iv		
1253.801	Si ii	1253.811	ISM	1542.267	Ni iv		
1253.980	Ni v			1542.650	Ni iv		
1254.025	Ni v			1542.698	Fe iv		
1254.191	Ni v			1542.884	Ni iv		
1254.417	Ni v			1543.236	Fe v		
1255.214	Zn iv			1543.372	Ni iv		
1255.430	Fe vi			1543.422	Ni iv		
1255.723	Ni v			1543.567	Ni iv		
1255.743	Ni v			1544.075	Ni iv		
1255.799	Ni v			1544.232	Fe v		
1256.005	Ni v			1544.486	Fe iv		
1256.049	Ni v			1544.634	Fe iv		
1256.218	Ni v			1544.749	Fe iv		
1256.289	Ni v			1545.394	Ni iv		
1256.368	Ni v			1545.442	Fe iv		
1256.444	Ni v			1546.233	Ni iv		
1256.847	Ni v			1546.404	Fe iv		
1256.905	Ni v			1547.585	Fe iv		
1257.626	Ni v			1547.615	Fe iv		
1258.031	Ni v			1548.057	Ni iv		
1258.254	Ni v			1548.130	C iv	1548	203.ISM
1258.539	Ni v			1548.203	C iv		
1258.881	Fe vi			1549.957	Fe iv		
1259.027	Ni v			1550.700	C iv	1550	772.ISM
1259.119	Ni v			1550.772	C iv		
1259.187	Ni v			1550.907	Fe v		
1259.459	Fe ii	1259.519	ISM	1552.208	Fe iv		
1259.504	Fe ii	1259.519	ISM	1552.349	Fe iv		
1259.587	Ni v			1552.705	Fe iv		
1259.722	Ni v			1553.079	Fe iv		
1260.316	Fe vi			1553.171	Fe iv		
1260.367	Si ii	1260.422	ISM	1553.296	Fe iv		
1260.407	Si ii	1260.422	ISM	1553.429	Ni iv		
1260.409	Ni v			1554.219	Fe v		
1260.746	Fe vi			1554.672	Fe iv		
1261.058	Fe vi			1554.804	Ni iv		
1261.225	Ni v			1555.447	Fe v		
1261.255	Ni v			1555.948	Fe iv		
1261.327	Ni v			1556.062	Fe iv		
1261.414	Ni v			1557.182	Fe iv		
1261.760	Ni v			1557.281	Ni iv		
1262.539	Ni v			1557.310	Fe v		
1262.550	Ni v			1557.456	Fe iv		
1263.282	Ni v			1557.647	Fe v		
1263.330	Ni v			1558.115	Fe v		
1264.251	Ni v			1558.123	Fe v		
1264.446	Ni v			1558.670	Fe iv		
1264.501	Ni v			1558.788	Fe iv		
1264.768	Ni v			1558.897	Fe iv		
1264.937	Ni v			1559.113	Fe iv		
1265.671	Ni v			1559.188	Fe iv		
1265.725	Ni v			1559.921	Ni iv		
1265.872	Fe vi			1560.269	Fe iv		
1266.103	Fe vi			1560.507	Fe iv		
1266.111	Ni v			1560.708	Fe iv		
1266.113	Ni iv			1561.205	Fe v		

Table 5. continued.

$\lambda_{\text{rest}} / \text{\AA}$	ion	$\lambda_{\text{theo}} / \text{\AA}$	comment	$\lambda_{\text{rest}} / \text{\AA}$	ion	$\lambda_{\text{theo}} / \text{\AA}$	comment
1266.129	Fe v			1561.301	Fe iv		
1266.131	Ni v			1561.352	Fe iv		
1266.408	Ni v			1562.261	Fe iv		
1266.522	Fe v			1562.460	Fe iv		
1266.706	Ni v			1562.752	Fe iv		
1266.876	Ni v			1563.137	Fe iv		
1267.234	Ni v			1563.231	Fe iv		
1267.277	Zn iv			1563.583	Fe iv		
1267.291	Ni v			1563.756	Fe iv		
1267.307	Ni v			1563.939	Fe v		
1267.421	Co v			1564.272	Ni iv		
1267.802	Ni v			1564.602	Fe iv		
1267.875	Ni v			1564.638	Fe iv		
1268.178	Ni v			1564.781	Fe iv		
1268.873	Ni v			1565.865	Fe iv		
1269.226	Ni v			1566.257	Fe iv		
1269.387	Ni v			1566.334	Fe iv		
1269.785	Fe v			1566.466	Fe iv		
1269.846	Ni v			1566.568	Fe iv		
1270.198	Ni v			1566.684	Fe v		
1270.472	Fe v			1566.752	Fe iv		
1270.677	Ni v			1567.000	Ni iv		
1270.760	Fe iv			1567.046	Fe iv		
1271.099	Fe vi			1567.956	Fe iv		
1271.275	Ni v			1568.276	Fe iv		
1271.428	Ni v			1568.416	Fe v		
1271.574	Ni v			1568.716	Fe iv		
1272.035	Ni v			1569.222	Fe iv		
1272.066	Fe vi			1569.346	Fe iv		
1272.627	Ni v			1569.977	Fe v		
1272.660	Ni v			1570.178	Fe iv		
1272.692	Ni v			1570.416	Fe iv		
1272.749	Ni v			1571.244	Fe iv		
1272.856	Fe vi			1573.590	Fe iv		
1272.872	Ni v			1574.606	Fe iv		
1273.204	Ni v			1574.739	Fe iv		
1273.731	Ni v			1575.098	Fe iv		
1273.827	Ni v			1575.188	Fe iv		
1273.898	Ni v			1575.407	Fe iv		
1274.264	Ni v			1575.620	Fe iv		
1274.522	Ni v			1575.756	Fe iv		
1275.898	Ni v			1576.216	Fe v		
1276.072	Ni v			1576.437	Fe iv		
1276.428	Ni v			1577.205	Fe iv		
1276.877	Fe vi			1577.781	Fe iv		
1276.958	Ni v			1578.023	Fe iv		
1277.079	Zn iv			1578.612	Fe iv		
1277.170	Ni v			1578.740	Fe iv		
1277.310	Fe vi			1579.240	Fe iv		
1277.591	Ni vi			1579.378	Fe iv		
1278.292	Fe vi			1580.243	Fe iv		
1278.390	Ni v			1581.174	Fe iv		
1278.874	Ni v			1581.464	Fe iv		
1279.046	Ni v			1582.351	Ni iv		
1279.325	Ni v			1583.045	Ni iv		
1279.592	Fe v			1583.598	Fe iv		
1279.720	Ni v			1583.961	Fe iv		
1279.920	Ni v			1584.117	Fe iv		
1280.115	Ni v			1584.304	Ni iv		
1280.138	Ni v			1584.337	Fe v		

Table 5. continued.

$\lambda_{\text{rest}} / \text{\AA}$	ion	$\lambda_{\text{theo}} / \text{\AA}$	comment	$\lambda_{\text{rest}} / \text{\AA}$	ion	$\lambda_{\text{theo}} / \text{\AA}$	comment
1280.267	Ni v			1584.367	Fe v		
1280.295	Ni v			1584.382	Fe v		
1280.470	Fe v			1584.535	Fe v		
1281.220	Ni v			1584.985	Fe iv		
1281.281	Ni v			1585.113	Fe iv		
1281.649	Fe v			1585.304	Fe iv		
1282.060	Fe v			1585.658	Fe v		
1282.201	Ni v			1585.838	Fe iv		
1282.270	Ni v			1585.861	Fe iv		
1282.452	Fe vi			1587.586	Fe iv		
1282.724	Ni v			1588.901	Fe v		
1283.185	Ni v			1589.012	Fe v		
1283.386	Fe vi			1589.393	Fe v		
1283.613	Fe v			1590.616	Fe iv		
1283.949	Ni v			1590.864	Fe iv		
1283.979	Ni v			1591.065	Fe iv		
1284.055	Ni v			1591.508	Fe iv		
1284.111	Fe v			1591.802	Fe iv		
1284.475	Ni v			1591.875	Fe iv		
1284.566	Ni v			1591.878	Fe iv		
1285.362	Fe vi			1591.926	Ni iv		
1285.793	Ni v			1592.050	Fe iv		
1285.916	Fe v			1592.329	Fe iv		
1286.096	Ni v			1593.079	Fe iv		
1286.235	Fe vi			1593.702	Fe v		
1287.028	Ni v			1594.925	Fe iv		
1287.107	Fe v			1595.138	Zn iv		
1287.553	Ni v			1595.795	Fe iv		
1287.628	Ni v			1596.061	Fe iv		
1287.808	Ni v			1596.368	Fe v		
1288.172	Fe v			1596.670	Fe iv		
1288.263	Cr iv			1597.404	Fe iv		
1288.384	Ni v			1597.907	Fe iv		
1288.515	Ni v			1598.011	Fe iv		
1288.789	Fe v			1598.349	Fe iv		
1288.833	Fe v			1598.541	Fe iv		
1288.955	Fe v			1598.563	Fe v		
1289.427	Ni v			1598.823	Fe v		
1289.773	Ni v			1599.841	Fe v		
1290.398	Ni v			1600.497	Fe iv		
1291.187	Fe v			1600.582	Fe iv		
1291.880	Ni v			1601.261	Fe iv		
1292.005	Ni v			1601.502	Fe iv		
1292.076	Ni v			1601.652	Fe iv		
1292.469	Cr iv			1601.670	Fe iv		
1293.126	Fe v			1601.819	Fe iv		
1293.163	Ni v			1601.898	Fe iv		
1293.306	Fe v			1602.061	Fe iv		
1293.382	Fe v			1603.177	Fe iv		
1294.539	Ni v			1603.731	Fe iv		
1294.545	Si iii			1604.670	Fe iv		
1295.201	Fe vi			1604.875	Fe iv		
1295.300	Ni v			1605.679	Fe iv		
1295.797	Ni v			1605.764	Al iii		
1296.154	Ni v			1605.970	Fe iv		
1296.203	Ni v			1606.336	Fe iv		
1296.726	Si iii			1606.972	Fe iv		
1296.734	Fe vi			1607.689	Fe iv		
1296.872	Fe vi			1607.833	Fe v		
1297.549	Fe v			1608.381	Fe ii	1608	451.ISM

Table 5. continued.

$\lambda_{\text{rest}} / \text{\AA}$	ion	$\lambda_{\text{theo}} / \text{\AA}$	comment	$\lambda_{\text{rest}} / \text{\AA}$	ion	$\lambda_{\text{theo}} / \text{\AA}$	comment
1298.738	Ni v			1608.434	Fe ii	1608	451.ISM
1298.892	Si iii			1608.850	Fe iv		
1298.946	Si iii			1609.004	Fe iv		
1300.341	Fe iv			1609.100	Fe iv		
1300.608	Fe v			1609.105	Fe iv		
1300.979	Ni v			1609.835	Fe iv		
1301.149	Si iii			1609.924	Fe iv		
1301.174	Fe vi			1610.035	Fe iv		
1301.265	Ni v			1610.467	Fe iv		
1301.585	Fe vi			1610.847	Fe iv		
1301.614	Ni iv			1611.014	Fe iv		
1301.707	N iv			1611.203	Fe iv		
1301.707	N iv			1611.812	Al iii		
1301.800	Fe vi			1611.871	Al iii		
1301.821	O iii			1611.985	Fe iv		
1301.958	O i	1302.168	ISM	1612.066	Ni iv		
1302.109	O i	1302.168	ISM	1612.230	Ni iv		
1302.152	O i	1302.168	ISM	1612.794	Fe iv		
1302.251	Ni v			1613.321	Fe iv		
1302.387	Ni v			1613.325	Fe v		
1302.787	Fe v			1613.340	Ni iv		
1302.848	Ni v			1613.567	Fe iv		
1303.083	Fe v			1613.642	Fe iv		
1303.323	Si iii			1613.644	Fe iv		
1303.326	Ni v			1613.991	Fe iv		
1303.487	Fe v			1614.049	Fe iv		
1303.523	Fe v			1614.189	Fe v		
1303.983	Ni v			1614.645	Fe iv		
1304.311	Si ii	1304.370	ISM	1615.004	Fe iv		
1304.357	Si ii	1304.370	ISM	1615.605	Fe iv		
1304.521	Cr iv			1616.128	Fe iv		
1304.647	P ii	1304.675	ISM	1616.681	Fe iv		
1304.814	Fe v			1617.040	Fe v		
1304.848	O iii			1617.259	Fe iv		
1304.870	Ni v			1617.685	Fe iv		
1305.066	Ni v			1618.574	Fe iv		
1305.696	Ni v			1619.022	Fe iv		
1305.818	C ii	1305.884	ISM	1619.137	Fe iv		
1305.962	Ni v			1620.086	Fe v		
1306.080	Fe v			1620.186	Fe iv		
1306.238	Ni v			1620.914	Fe iv		
1306.624	Ni v			1621.139	Fe iv		
1306.701	Ni v			1621.184	Fe iv		
1307.219	Fe v			1621.569	Fe iv		
1307.424	Fe v			1621.849	Fe iv		
1307.603	Ni v			1622.122	Fe iv		
1307.779	Ni v			1623.386	Fe iv		
1308.233	Cr iv			1623.532	Fe iv		
1308.606	Ni v			1624.255	Fe v		
1308.669	Ni v			1624.912	Fe iv		
1309.140	Fe v			1625.271	Fe v		
1309.206	Cr iv			1625.653	S iv		
1309.262	Fe v			1626.085	Fe v		
1309.519	Fe v			1626.268	Fe iv		
1309.653	Ni v			1626.467	Fe iv		
1309.689	Ni v			1626.904	Fe iv		
1309.910	Fe vi			1627.236	Fe iv		
1310.092	Ni v			1627.314	Fe iv		
1310.252	Ni v			1627.442	Fe iv		
1311.027	Ni v			1628.211	Ni v		

Table 5. continued.

$\lambda_{\text{rest}} / \text{\AA}$	ion	$\lambda_{\text{theo}} / \text{\AA}$	comment	$\lambda_{\text{rest}} / \text{\AA}$	ion	$\lambda_{\text{theo}} / \text{\AA}$	comment
1311.106	Ni v			1628.544	Fe iv		
1311.238	Fe v			1629.045	Fe iv		
1311.529	Cr iv			1629.126	Fe iv		
1311.560	Ni v			1629.203	Fe iv		
1311.828	Fe v			1629.291	Fe iv		
1311.935	Zn iv			1630.110	Fe iv		
1312.017	Ni v			1630.178	Fe iv		
1312.040	Ni iv			1630.380	Ni v		
1312.646	Ni v			1630.678	Fe iv		
1312.717	Ni v			1631.077	Fe iv		
1312.718	Ni v			1631.091	Fe iv		
1313.280	Ni v			1631.557	Fe iv		
1314.314	Ni v			1631.667	Fe iv		
1314.330	Ni v			1632.082	Fe iv		
1314.349	Ni v			1632.408	Fe iv		
1314.401	Ni v			1633.074	Fe iv		
1314.492	Fe v			1634.003	Fe iv		
1314.537	Sn iv			1634.757	Fe iv		
1314.682	Ni v			1635.399	Fe iv		
1314.909	Ni v			1635.832	Fe iv		
1314.992	Ni v			1638.070	Fe iv		
1315.232	Ni v			1638.297	Fe iv		
1315.296	Ni iv			1639.400	Fe iv		
1315.585	Fe v			1640.042	Fe iv		
1315.653	Ni v			1640.155	Fe iv		
1315.834	Cr iv			1640.419	He ii		
1316.281	Ni v			1640.784	Fe iv		
1316.892	Ni v			1641.604	Fe iv		
1317.034	Ni v			1641.864	Fe iv		
1317.067	Ni v			1642.776	Fe iv		
1317.447	Ni v			1642.875	Fe iv		
1317.731	Fe vi			1644.939	Fe iv		
1317.837	Fe v			1644.942	Fe iv		
1317.957	Ni v			1647.093	Fe iv		
1318.145	Ni v			1647.233	Fe iv		
1318.327	Ni v			1649.188	Fe iv		
1318.355	Fe v			1649.996	Fe iv		
1318.362	Fe v			1650.096	Fe iv		
1318.515	Ni v			1651.576	Fe iv		
1319.164	Ni v			1652.902	Fe iv		
1319.319	Ni iv			1653.407	Fe iv		
1319.693	Cr iv			1654.301	Fe iv		
1319.754	Ni v			1654.744	Fe v		
1319.815	Ni v			1656.111	Fe iv		
1320.224	Ni v			1656.652	Fe iv		
1320.298	Fe v			1657.134	Fe iv		
1320.409	Fe v			1657.370	Fe iv		
1320.700	Ni v			1657.828	Fe iv		
1320.702	Zn iv			1658.246	Fe iv		
1320.803	Fe iv			1658.433	Fe iv		
1320.889	Ni v			1659.004	Fe iv		
1321.243	Ni v			1660.103	Fe iv		
1321.341	Fe v			1661.573	Fe iv		
1321.489	Fe v			1662.319	Fe iv		
1321.849	Fe v			1662.519	Fe iv		
1322.314	Zn iv			1663.543	Fe iv		
1322.426	Zn iv			1664.763	Mn iv		
1323.038	Ni iv			1664.772	Mn iv		
1323.098	Fe v			1664.936	Fe iv		
1323.271	Fe v			1667.002	Fe iv		

Table 5. continued.

$\lambda_{\text{rest}} / \text{\AA}$	ion	$\lambda_{\text{theo}} / \text{\AA}$	comment	$\lambda_{\text{rest}} / \text{\AA}$	ion	$\lambda_{\text{theo}} / \text{\AA}$	comment
1323.553	Ni v			1667.758	Fe iv		
1323.562	Ni v			1668.065	Fe iv		
1323.977	Ni v			1668.119	Fe iv		
1324.000	Ni v			1668.177	Fe iv		
1324.247	Co v			1669.602	Fe iv		
1324.286	Fe vi			1669.666	Fe iv		
1324.286	Ni v			1669.813	Fe iv		
1324.407	Fe v			1670.706	Fe iv		
1324.466	Ni v			1670.714	Al ii	1670	790.ISM
1324.742	Ni v			1670.770	Al ii	1670	790.ISM
1325.019	Cr iv			1670.786	Fe iv		
1325.068	Ni v			1671.041	Fe iv		
1325.464	Ni vi			1671.057	Fe iv		
1325.782	Fe v			1672.014	Ni v		
1327.101	Fe v			1672.209	Fe iv		
1327.390	Ni v			1672.428	Fe iv		
1327.466	Ni v			1672.861	Fe iv		
1327.556	Ni v			1673.054	Fe iv		
1327.656	Ni v			1673.371	Fe iv		
1327.938	Ni v			1673.679	Fe iv		
1328.025	Ni v			1675.660	Fe iv		
1328.849	Fe iv			1676.421	Ni iv		
1329.020	Fe v			1676.511	Fe iv		
1329.177	Fe vi			1676.786	Fe iv		
1329.186	Ni vi			1677.123	Fe iv		
1329.186	Ni vi			1681.286	Fe iv		
1329.358	Ni v			1681.356	Fe iv		
1329.871	Fe iv			1681.945	Fe iv		
1329.962	V iv			1687.437	Fe iv		
1330.049	Ni v			1687.529	Fe iv		
1330.405	Fe v			1687.532	Fe iv		
1330.546	Fe v			1687.683	Fe iv		
1330.971	Fe vi			1687.751	Fe iv		
1331.639	Fe v			1688.388	Mn v		
1331.992	Ni v			1689.610	Fe iv		
1332.415	Cr iv			1690.321	Fe iv		
1332.784	Ni v			1690.635	Fe iv		
1332.846	Ni iv			1695.036	Fe iv		
1332.910	Ni iv			1695.361	Fe iv		
1333.010	Ni v			1695.772	Fe iv		
1333.179	Zn iv			1698.716	Mn iv		
1333.328	Ni v			1698.884	Fe iv		
1333.572	Ni v			1700.407	Fe iv		
1333.958	Ni v			1700.816	Fe iv		
1334.169	Ni v			1701.003	Fe iv		
1334.280	Ni v			1701.478	Fe iv		
1334.476	C ii	1334.532	ISM	1704.185	Fe iv		
1334.521	C ii	1334.532	ISM	1704.930	Fe iv		
1334.966	Ni v			1707.609	Fe iv		
1335.593	C ii	1335.662	ISM	1708.570	Fe iv		
1335.623	Ni iv			1709.809	Fe iv		
1335.639	C ii	1335.708	ISM	1711.412	Fe iv		
1335.640	C ii	1335.662	ISM	1712.759	Fe iv		
1335.686	C ii	1335.708	ISM	1717.104	Fe iv		
1335.757	Fe v			1717.895	Fe iv		
1336.039	Fe v			1718.163	Fe iv		
1336.136	Ni v			1718.407	Fe iv		
1336.205	Cr iv			1718.550	N iv		
1336.536	Ni v			1719.467	Fe iv		
1336.621	Ni v			1722.526	Si iv		

Table 5. continued.

$\lambda_{\text{rest}} / \text{\AA}$	ion	$\lambda_{\text{theo}} / \text{\AA}$	comment	$\lambda_{\text{rest}} / \text{\AA}$	ion	$\lambda_{\text{theo}} / \text{\AA}$	comment
1336.870	Zn iv			1722.562	Si iv		
1337.006	Ni v			1722.710	Fe iv		
1337.041	Ni v			1723.958	Fe iv		
1337.286	Fe v			1724.055	Fe iv		
1337.692	Fe vi			1724.263	Fe iv		
1337.769	Fe v			1724.641	Fe iv		
1337.793	Fe vi			1725.627	Fe iv		
1337.793	Ni vi			1725.673	Fe iv		
1337.961	Ni iv			1727.376	Si iv		
1338.615	O iv			1730.331	Fe iv		
1338.808	Fe v			1731.233	Fe iv		
1339.050	Ni v			1735.728	Fe iv		
1339.170	Cr iv			1740.158	Fe iv		
1339.569	Cr iv			1751.756	Fe iv		
1339.674	Ni iv			1753.085	Fe iv		
1339.691	Fe v			1755.643	Cr iv		
1339.791	Cr iv			1761.078	Fe iv		
1340.154	Zn iv			1764.919	Fe iv		
1340.332	Ni v			1780.711	Fe iv		
1341.074	Ni v			1783.070	Fe iv		
1342.176	Ni v			1792.113	Fe iv		
1342.918	Ni v			1793.847	Fe iv		
1342.990	O iv			1793.880	Fe iv		
1343.109	Fe v			1793.880	Ge v		
1343.113	Fe v			1796.950	Fe iv		
1343.118	Ni v			1805.322	Fe iv		
1343.118	Ni v			1809.737	Fe iv		
1343.142	Fe v			1810.061	Fe iv		
1343.514	O iv			1827.979	Fe iv		
1343.626	Ni v			1840.146	Cr iv		
1343.748	Zn iv			1840.244	Fe iv		
1343.896	Ni v			1850.575	Fe iv		
1344.091	Ni iv			1854.714	Al iii		
1344.120	Zn iv			1862.787	Al iii		
1345.401	Ni v			1869.632	Fe iv		
1345.603	Fe v			1870.959	Fe iv		
1345.656	Fe v			1872.761	Fe iv		
1345.723	Ni iv			1873.891	Cr iv		
1346.094	Ni v			1873.935	Fe iv		

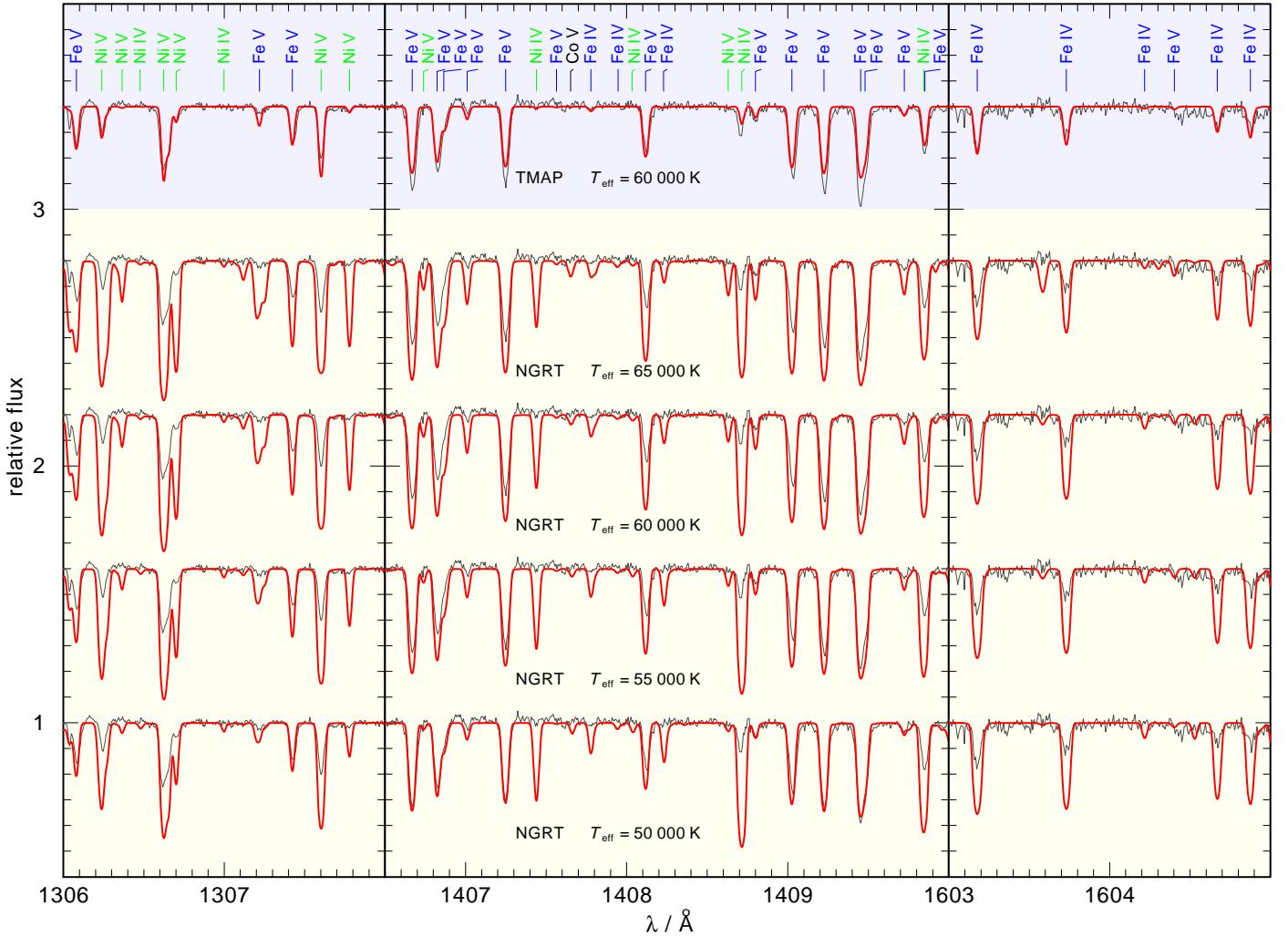


Fig. 23. Comparison of our model spectra (all calculated with $\log g = 7.60$) with the STIS observation. Top: Final homogeneous model (TMAP). The stratified NGRT models have $T_{\text{eff}} = 65\,000 \text{ K}$, $60\,000 \text{ K}$, $55\,000 \text{ K}$, and $50\,000 \text{ K}$ (from top to bottom). The lines in the models are marked.